

Coupled Geochemical and Nano-Petrophysical Study of The Spraberry-

Wolfcamp Trend

West Texas, U.S.A.

by

RYAN P. QUINTERO

Presented to the Faculty of the Graduate School of
The University of Texas at Arlington in Partial Fulfillment
of the Requirements
for the Degree of

MASTER OF SCIENCE IN EARTH AND ENVIRONMENTAL SCIENCES

THE UNIVERSITY OF TEXAS AT ARLINGTON

DECEMBER 2016

Copyright © by Ryan Quintero 2016

All Rights Reserved



Acknowledgements

I would like to thank Element Petroleum for being so kind in donating samples and available data, without this I would not have been able to complete this research. Much appreciation to Drillinginfo, who made it so simple to gather data and construct figures for this thesis. Weatherford Laboratories was also more than helpful by providing methods and procedures for geochemical analyses and XRD. To my advisor and committee, Dr. Qinhong Hu, Dr. John Wickham, and Dr. Andrew Hunt, I am indebted to for their guidance. Thanks to the Earth and Environmental Sciences department as a whole for giving me the opportunity to expand my knowledge and educational prowess. To the whole University of Texas at Arlington I give thanks for being so accommodating in every way. Last but definitely not least, thank you to my mother, father, sister, relatives, and friends for giving me the support and invaluable encouragement during my time in graduate school.

November 9, 2016

Abstract

Coupled Geochemical and Nano-Petrophysical Study of The Spraberry-
Wolfcamp Trend
West Texas, U.S.A.

Ryan Quintero, MS

The University of Texas at Arlington, 2016

Supervising Professor: Qinhong Hu

With the rise in interest of unconventional plays, efforts have moved to understand these formations across 12 orders of magnitude through nm-km scale. Recent work by others has shown the importance of the nanometer range due to the fact this is the predominant pore size within shales. In attempt to understand nanopore structure and production behavior within a shale unconventional reservoir, a number of complementary experimental methods must be employed.

This research involves the use of wettability droplet analysis for micron scale assessment of wetting properties and Mercury Intrusion Capillary Pressure (MICP) analysis for pore structure characterization within the Spraberry and Wolfcamp Formations of the Permian Basin in west Texas. In conjunction with pyrolysis and X-ray diffraction data from two wells, total organic carbon (TOC), thermal maturation, and mineralogy are considered for the development of the pore system. The Spraberry Formation was found to contain a larger porosity, higher permeability, and lower tortuosity than the Wolfcamp. The two formations also showed different pore size

distributions, with the Spraberry containing more intra- and inter-pores (10-100 nm) while the Wolfcamp containing more organic sized pores (predominantly at 5-10 nm). Mineralogy differences between these shales showed no strong relationship with pore sizes distribution nor maturation. Values of S1 (volatile hydrocarbon content) from pyrolysis analyses showed the strongest relationship with pore sizes. As S1 values increased, the higher porosity increased; this rise in porosity is seen predominantly within organic pore sizes. Production data from the Rogers #3804 and Wright #44 are compared to Jarvie's oil generation crossover line (S1 vs. TOC). This crossover line accurately predicts the historical trend of these two wells.

Table of Contents

Acknowledgements	iii
Abstract	iv
List of Illustrations	viii
List of Tables	x
Chapter 1 Introduction	1
Chapter 2 Geologic Setting	5
Chapter 3 Methods	9
3-1 Acquisition of Samples	9
3-2 Wettability	16
3-3 Mercury Injection Capillary Pressure (MICP)	16
Procedure for MICP Tests	19
3-4 Pyrolysis and XRD	20
3-5 Production Data	21
Chapter 4 Results	22
4-1 Wettability	22
4-2 Mercury Intrusion Capillary Pressure	27
4-3 Mineralogy	32
4-4 Pyrolysis	35
4-5 Production	39
Chapter 5 Discussion and Conclusions	43
5-1 Wettability	43
5-2 Pore Structure vs. Mineralogy	43
5-3 Organic Geochemistry vs. Mineralogy	45
5-4 Pore Structure vs. Organic Geochemistry	46

5-5 Production Data.....	50
5-6 Particle Size Distribution	50
5-7 Conclusion.....	51
5-8 Recommendations	52
Appendix A Methods and Procedures for Geochemical Analysis at	
Weatherford Laboratories	53
Rock Sample Preparation.....	54
Total Organic Carbon	54
Programmed Pyrolysis (Rock-Eval II, Rock-Eval VI, Source Rock	
Analyzer)	54
Vitrinite Reflectance and Visual Kerogen Assessment.....	55
Appendix B Methods and Procedures of X-Ray Diffraction Analysis at	
Weatherford Laboratories	56
References.....	61
Biographical Information	66

List of Illustrations

Figure 1-1 Spraberry-Wolfcamp Trend (BEG, 2008)	3
Figure 1-2 Partial Stratigraphic Column of the Midland and Delaware Basins (Murchison Oil & Gas, 2010).....	4
Figure 2-1 Permian Sub-Basins (Henry, 2012).....	6
Figure 2-2 Stratigraphic Column of Spraberry–Wolfcamp Trend (Guevara, 2006).....	7
Figure 2-3 Well log of Rogers #3804 Sample Interval	8
Figure 3-1 Well location (Drilling Info, 2016).....	10
Figure 3-2 Sample Photos Upon Arrival: (1) Zoomed out (2) Zoomed in (scale bars are all shown on the pictures) (A) Spra1; (B) Spra2; (C) Spra3; (D) Spra4; (E) Wolf1; (F) Wolf2; (G) Wolf3; (H) Wolf4; (I) Wolf5; (J) Wolf6; (K) Wolf7; (L) Wolf8.....	14
Figure 4-1 Example of Chosen Inflection Points (Sample-Spra2)	28
Figure 4-2 Pore Throat Diameter vs. Pore Throat Distribution in Spra2&4 (Lower Spraberry)	31
Figure 4-3 Pore Throat Diameter vs. Pore Throat Distribution in Wolf1-8 (Wolfcamp Formation).....	31
Figure 4-4 Mineralogy of Rogers #3804 Well in Weight Percent	33
Figure 4-5 Mineralogy of Wright 44 #1E Well in Weight Percent.....	33
Figure 4-6 Samples from both Rogers #3804E and Wright 44#1E Plotted on a Ternary Diagram for sCore Lithofacies Classification Scheme for Organic Mudstones Proposed by Schlumberger (2014). Spraberry: triangle, Wolfcamp: square. Sample Formations not known for Wright. (filled for Roger, open for Wright).....	34
Figure 4-7 S1 vs. Depth in Rogers #3804E and Wright 44#1E Wells.....	37
Figure 4-8 S1 vs. TOC with reference to Jarvie’s Crossover Generation Index in Rogers #3804E and Wright 44#1E Wells	38

Figure 4-9 Monthly Production Data: (A) Rogers #3804E; (B) Wright #44E; (C) Garrett Reed 37-48; (D) Garrett-Reed 37-48 (Daily Production). (Drilling Info, 2016). ...	42
Figure 5-1 Pore Size Distribution vs. Mineralogy in Spra2	44
Figure 5-2 Pore Size Distribution vs. Mineralogy in Wolf8	44
Figure 5-3 Pore Size Distribution vs. Mineralogy in Wolf 4 & 5	45
Figure 5-4 Total Organic Carbon vs. Weight Percent of Clay (Data from <20% and >40% Clay).....	46
Figure 5-5 S1 vs. Porosity in Rogers #3804 Well	47
Figure 5-6 Organic Pore (2.7-50nm) Percentage relative to S1 Values	48
Figure 5-7 μm -Pore (1-50 μm) Percentage relative to S1 Values	48
Figure 5-8 Organic Pore (5-50nm) Percentage relative to S1 Values	49
Figure 5-9 Particle Size Distribution of Rogers Samples	51

List of Tables

Table 3-1 Location of Wells in Howard County, Texas	9
Table 3-2 Sample List from Well Rogers #3804	10
Table 3-3 Tests Performed on Each Sample at UTA.....	15
Table 4-1 Wettability Results	23
Table 4-2 Wettability Test Pictures	24
Table 4-3 MICP Results	30
Table 4-4 Geochemical data of both Rogers #3804 and Wright #44 Wells	36
Table 4-5 Well information for Three Wells.....	39

Chapter 1

Introduction

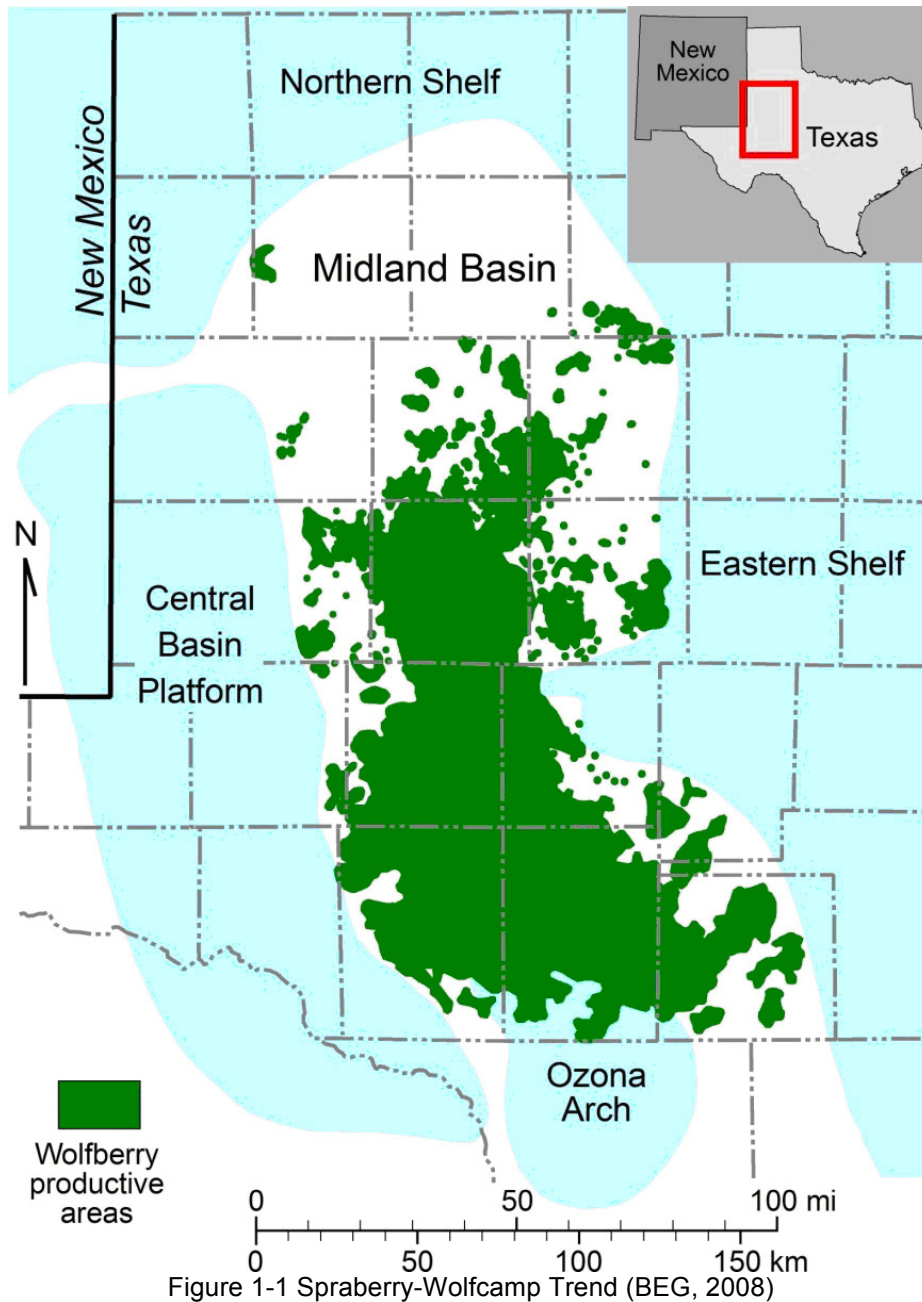
Throughout the history of the petroleum industry one of the main enigmas to plague producers is the problem of sharp production decline. Historically, once a well stopped producing economically, another well was drilled. New wells are needed to maintain the stable production level of a field. In modern times, completing an additional well is costly. Purchasing extra acreage is also expensive, if impossible at times. How to keep an already existing producing well at a high, constant rate has driven energy companies to pour much of their resources into the advancement of petroleum geoscience and engineering.

The Spraberry and Dean Formations are normally referred together as the Spraberry trend. It is a large area encompassing over 2500 mi² (Montgomery, 2000) (Figure 1-1). The Spraberry Trend lies in the Midland Basin located in the western portion of Texas. The Spraberry can be separated into two distinct lithological groups: the Upper and Lower Spraberry. The Lower Spraberry, as well as the Dean and Wolfcamp Formations, contains high levels of total organic carbon (TOC). This leads the oil and gas producers to simultaneously target all three of these plays creating the Spraberry or “Wolfberry” trend (Figure 1-2).

The Spraberry trend has been an important play within the Permian Basin since the 1950's. Together, the Spraberry and Dean Formations were projected to originally contain 40 billion barrels of oil. As of 2005, 1.2 billion barrels of oil have been produced from the Spraberry Formation out of the total 28.9 billion barrels extruded from the Permian Basin (Dutton et al., 2005). For nearly 50 years few petrophysical data had been gathered for the Spraberry Formation due to lack of technology for nano-pore structure studies, as well as economic downturns. Many recovery jobs were performed with

minimal scientific guidance, resulting in average recovery rates of 8-12% within the Spraberry Trend (Montgomery et al., 2000). At the turn of the century, rising oil prices fueled a new scientific initiative to understand the inner formational properties at work.

Recently, authors like King et al. (2015) and Lohr et al. (2015) have been comparing the relationship between kerogen maturation and pore size distribution. In this study, petrophysical [Mercury Intrusion Capillary Pressure (MICP), and wettability tests], geochemical (pyrolysis), and mineralogical (XRD) data will be used to better understand the factors which shape the pore systems of the “Wolfberry” Trend.



System	Delaware Basin		Midland Basin		
Permian		Dewey Lake		Dewey Lake	
		Rustler		Rustler	
		Salado		Salado	
		Castile			
	Delaware Mountain Group		Lamar	Whitenhorse	Tansill
			Bell Canyon		Yates
			Cherry Canyon		Seven Rivers
			Brushy Canyon		Queen
	Bone Spring		Avalon Shale	Word	Grayburg
			1st Bone Spring Sand		San Andres
				San Angelo	
			2nd Bone Spring Sand	Wolfberry / Wolffork	Clearfork
					Upper Spraberry
			3rd Bone Spring Sand		Lower Spraberry
		Wolfcamp	Dean		
		Wolfcamp			

Figure 1-2 Partial Stratigraphic Column of the Midland and Delaware Basins (Murchison Oil & Gas, 2010).

Chapter 2

Geologic Setting

The creation of the Permian Basin occurred during the collision of the South American and North American plates during Early Paleozoic time (Hickman, 2009). This collision formed the Marathon thrust belt, which is part of the larger Ouachita thrust system. In the resulting Marathon-Ouachita geosyncline, the Permian Basin formed within the foreland basin located north of the thrust belt (Hills, 1972). During Early Pennsylvanian time, strong reef and bank growth occurred throughout the basin. Along with increased tectonic activity in the area, uplift took place to separate the Permian Basin into two different sub basins: the Delaware Basin and the Midland Basin. This North-South trending area of uplift is called the Central Basin Platform, and is comprised of large carbonate reefs. This carbonate platform uplift is the main sediment provenance for the Midland Basin, along with large channels which supplied siliceous material.

In late Wolfcampian time, a slow advance of the seas began. This flood was the last time during the Permian when marine circulation was unrestricted and normal marine sediments were deposited. The Wolfcamp Formation, of Wolfcampian age, varies from fossiliferous limestone, dolomite, and shale which blankets all of the Permian sub-basins (Hills, 1972). These Wolfcampian reservoirs have individual thicknesses measured in tens of feet and occur in intervals approaching 1,000 ft. Drilling depths vary from 5,000 to 9,000 feet (Ball, 1995).

The Upper and Lower Spraberry Formations, along with the Dean Formation, are both of Leonardian age immediately overlying the Wolfcamp Formation. This Spraberry-Dean Play covers an area of about 150 mi long and 40–75 mi wide over the entire Midland Basin (Figure 2-1). The Spraberry Trend is bounded on the west by the Central Basin Platform, and on the east by the Eastern Shelf (Ball, 1995). Thickness of the

Spraberry Formation varies, but is consistently less than 1000' feet. Immediately older in age lies the Dean Formation, which only contains a thickness of between 100' and 200' feet. The Spraberry-Dean combination consists of mixed silicate and calcareous mudstone, siltstone, and fine sandstone reservoir facies deposited as turbidites in deep-water submarine fans with associated channel systems (Ball, 1995). Conventional reservoir traps for the area contain stratigraphic, stratigraphic-structural, and pure structural traps in deep-basinal clastic reservoirs of Lower Permian age (Ball, 1995). Unconventional production occurs within the high TOC-containing calcareous mudstones.



Figure 2-1 Permian Sub-Basins (Henry, 2012)

STRATIGRAPHIC COLUMN

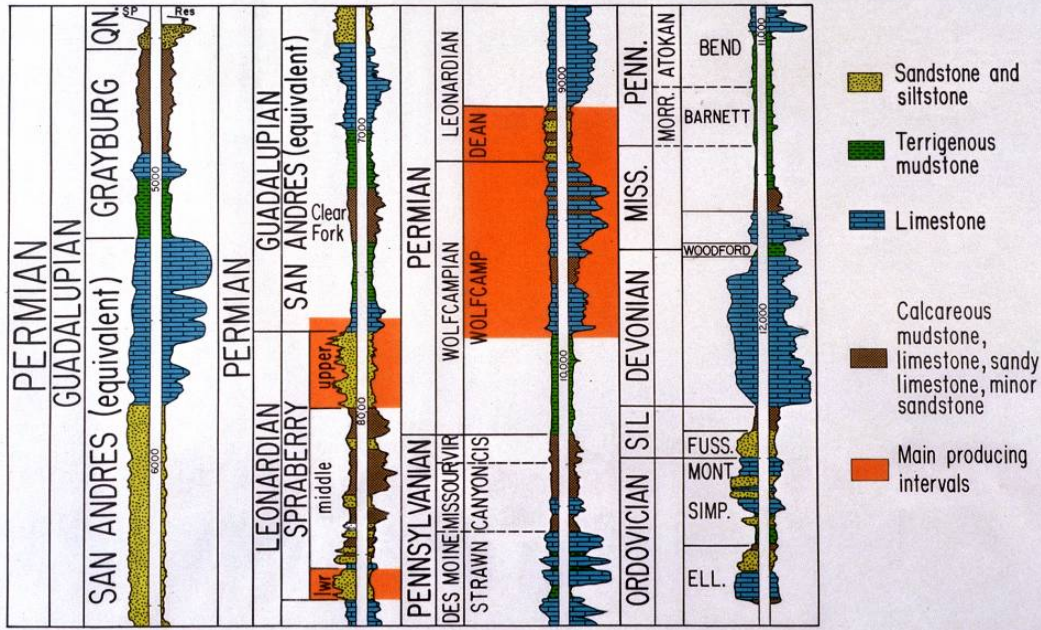


Figure 2-2 Stratigraphic Column of Spraberry–Wolfcamp Trend (Guevara, 2006)

Figure 2-3 presents an interval of a well log from Rogers #3804. The Lower Spraberry, Dean, and Wolfcamp Formations are shown. The shallowest top is shown to be named the Leonard, this is not a formally recognized formation name. This interval is rather a local age related naming convention for a carbonaceous unit just above the Dean sands.

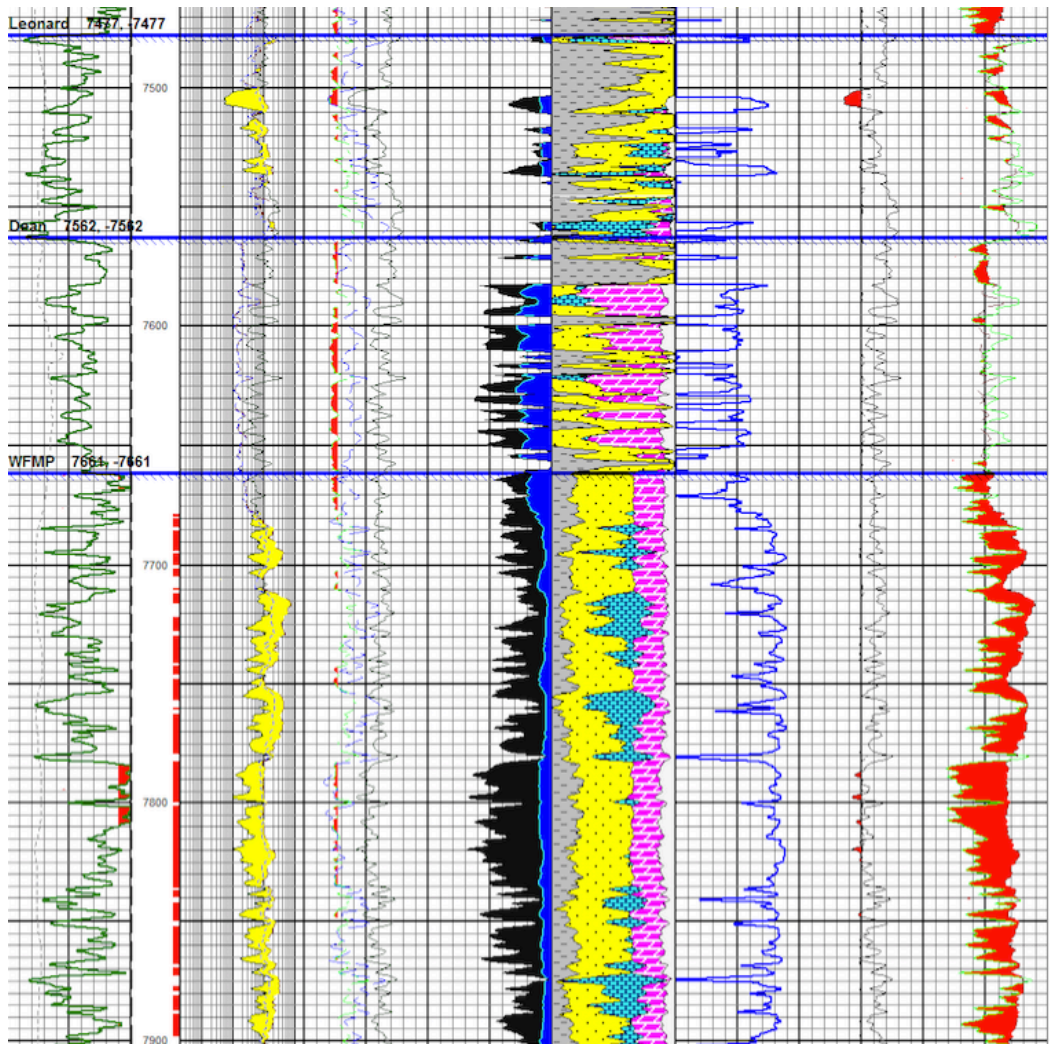


Figure 2-3 Well log of Rogers #3804 Sample Interval

Chapter 3

Methods

3-1 Acquisition of Samples

Core samples, as well as pyrolysis, XRD, and production data, were provided by Element Petroleum for the following three wells in Howard County: Rogers #3804E, Wright 44 #1E, and Garrett-Reed 37-48 4H (Table 3-1). Core fragment samples from Rogers #3804E are *only* available for additional experiments (wettability and MICP) at the University of Texas at Arlington (UTA). These samples came from 12 different depth intervals within the well (Table 3-2). Due to the spherical shape of the samples, as well as their limited size and weight, Table 3-3 displays which tests are performed on each sample in order to maximize use of all samples.

Table 3-1 Location of Wells in Howard County, Texas

Well Name	API #	Coordinates (Latitude and Longitude)
Rogers #3804E	42-227-37668	32.37482401N -101.55857422W
Wright 44 #1E	42-227-37738	32.4520231N -101.62483896W
Garrett-Reed 37-48 4H	42-227-37722	32.38243807N -101.53435036W

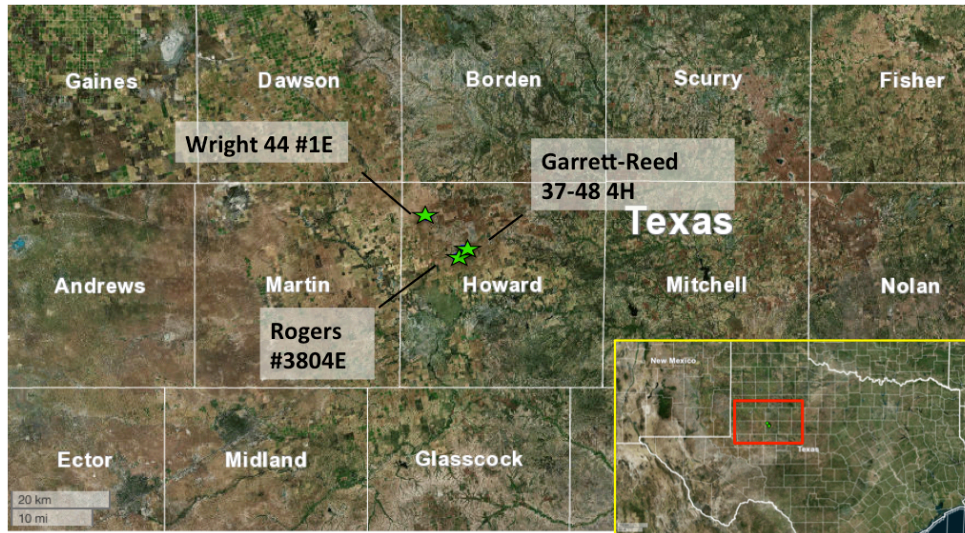
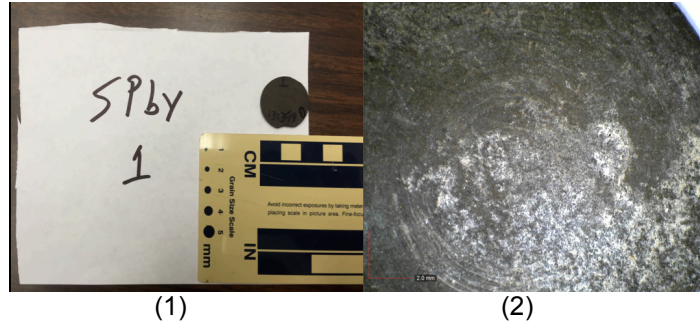


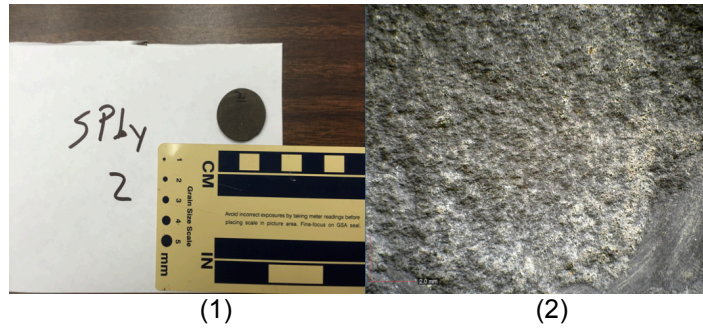
Figure 3-1 Well location (Drilling Info, 2016)

Table 3-2 Sample List from Well Rogers #3804

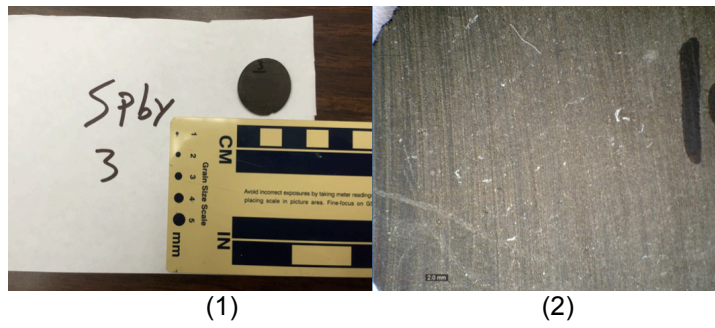
Sample ID	Depth (ft)	Formation	Diameter (cm)	Thickness (cm)	Sample Wt. (g)
Spra1	7,503	Lower Spraberry	2.324	0.191	1.627
Spra2	7,505	Lower Spraberry	2.315	0.241	1.697
Spra3	7,514	Lower Spraberry	2.285	0.428	2.655
Spra4	7,517	Lower Spraberry	2.336	0.608	3.939
Wolf1	7,665	Wolfcamp A	2.310	0.204	1.715
Wolf2	7,744	Wolfcamp A	2.280	0.184	1.547
Wolf3	7,787	Wolfcamp A	2.301	0.357	2.388
Wolf4	7,791	Wolfcamp A	2.319	0.336	3.009
Wolf5	7,808	Wolfcamp A	2.317	0.321	2.580
Wolf6	7,816	Wolfcamp A	2.340	0.326	3.181
Wolf7	7,820	Wolfcamp A	2.341	0.178	1.776
Wolf8	7,856	Wolfcamp A	2.328	0.665	5.133



(a)



(b)



(c)



(1)

(2)

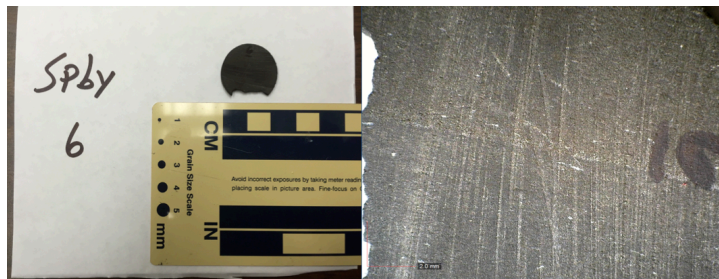
(d)



(1)

(2)

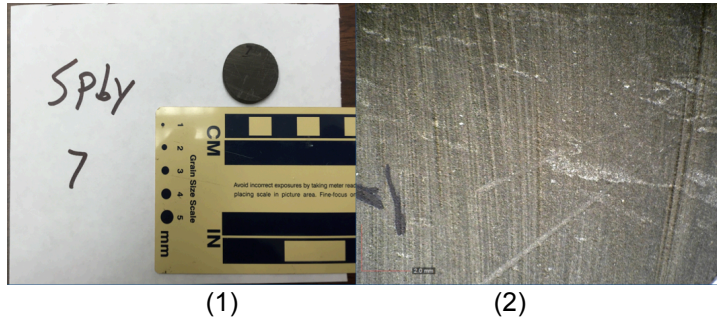
(e)



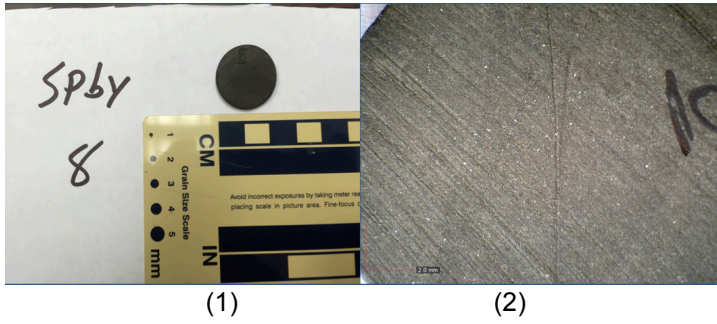
(1)

(2)

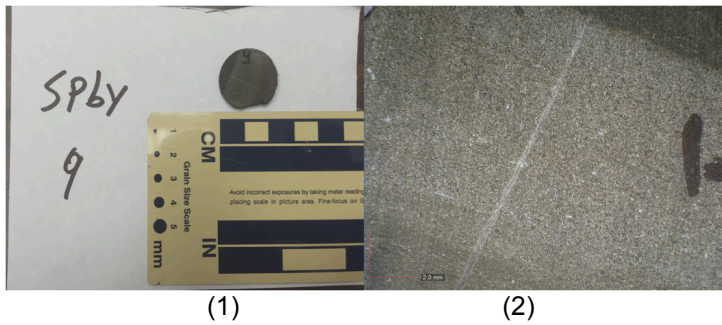
(f)



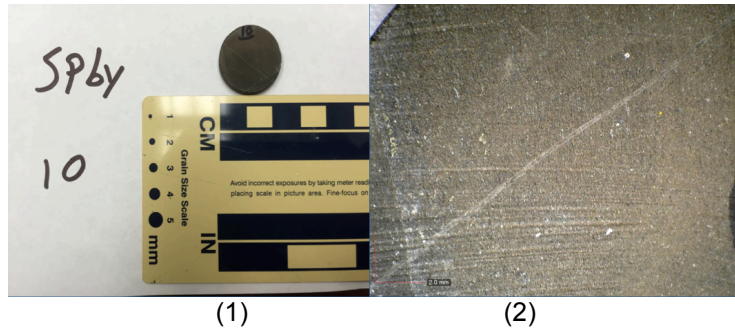
(g)



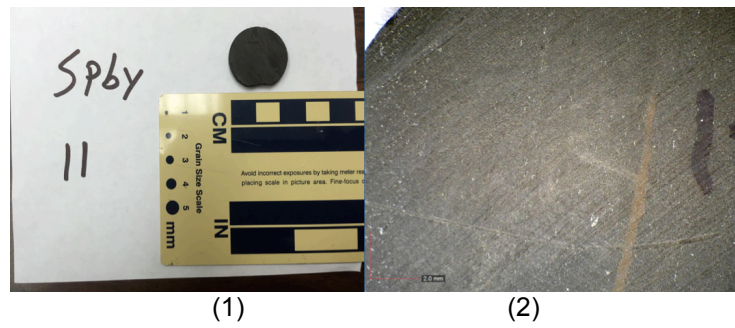
(h)



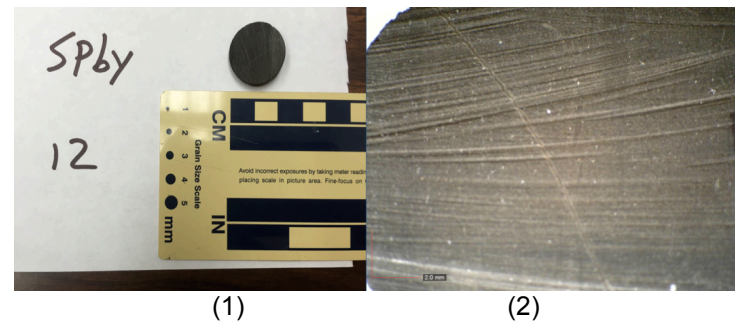
(i)



(j)



(k)



(l)

Figure 3-2 Sample Photos Upon Arrival: (1) Zoomed out (2) Zoomed in (scale bars are all shown on the pictures) (A) Spra1; (B) Spra2; (C) Spra3; (D) Spra4; (E) Wolf1; (F) Wolf2; (G) Wolf3; (H) Wolf4; (I) Wolf5; (J) Wolf6; (K) Wolf7; (L) Wolf8.

Following the photographic records, the samples were cut into smaller fragments. Due to their circular size and slimness, they were cut into quarters. These smaller sizes allowed for the use of several different tests. Many of the samples did not contain enough mass to perform both destructive wettability and MICP tests. Taking depth and mineralogy into account, the samples were divided up for use in either destructive wettability or MICP tests. Non-destructive wettability tests were performed on all samples. Following the cutting of the samples and before testing, they were placed in a 60°C drying oven in glass vials for at least 48 hrs. to complete the drying process. Once completely dry, the vials were removed from the oven and placed in a desiccator with low humidity to be cooled and stored before testing.

Table 3-3 Tests Performed on Each Sample at UTA

Associated Test					
Sample #	MICP	Fluid Type for Wettability			
		DI	API Brine	IPA 1%	N-Decane
Spra1		x	x	x	x
Spra2	x	x	x		
Spra3		x	x	x	x
Spra4	x	x	x	x	x
Wolf1	x	x	x		
Wolf2	x	x	x		
Wolf3		x	x	x	x
Wolf4	x	x	x	x	x
Wolf5	x	x	x		
Wolf6	x	x	x	x	x
Wolf7		x	x	x	x
Wolf8	x	x	x	x	x

3-2 Wettability

The wettability test observes the surface wetting characteristics of the sample and determines whether the shale is wetting or non-wetting to de-ionized (DI) water (water-wetting), API brine, 1% isopropyl alcohol (IPA), and n-decane (oil-wetting): API brine is water wetting but with a high salinity to mimic formation fluid, and 1% IPA is to achieve an intermediate surface tension between DI water and n-decane. This test was conducted with flat fragments to be polished for removal of cutting marks. One side of a fragment was used for DI water and the other side was used for API Brine, while the n-decane and IPA samples used their own respective sample and were discarded afterwards. One drop of fluid (2 μL) from a pipette was used to wet the surface of each sample to observe the spreading of the liquid. A qualitative number was assigned for the spreading behavior over 30 seconds; t, number one designating no spreading at all, while the number 10 representing perfect spreading of the fluid on the sample. In reference to the contact angle the bead makes at the sample surface interface, experiments given a value of one are equivalent to very high angles (e.g., $>100^\circ$) while samples given a value of 10 are very low (~ 0). Each sample was photographed and recorded during testing using a microscope camera.

3-3 Mercury Injection Capillary Pressure (MICP)

The MICP approach involves the use of non-wetting mercury applied at a pressure of up to 61,000 psia (420 Mpa) to overcome the capillary pressure and invade the pores of the shale samples. The instrument used (Micrometrics Autopore IV 9510, Norcross GA) for this research is located at the University of Texas at Arlington. Mercury Porosimetry is done by applying increasing levels of pressure to a sample surrounded by mercury (Zhou, 2010). As the pressure increases, the smaller the pore throat can be

invaded, thus creating a distribution curve of pore sizes (Hu and Ewing, 2014; Kaufmann, 2010). The range of pore sizes able to be detected is 2.8 nm to 50 μm in diameter for tight shale samples. This method is able to characterize a sample's particle and bulk density, porosity, total pore surface area, pore-throat distribution total volume, and median or mean pore diameters. Permeability and tortuosity can also be determined empirically (Katz and Thompson, 1986; Micrometrics, 2011; Hu and Ewing, 2014; Hu et al., 2015;).

The laws governing capillary pressure determine the capability of MICP approach (Hu et al., 2015a). Mercury is unique in that it acts as a non-wetting fluid in porous media, requiring external pressure to invade pore throats. The Washburn equation is used to determine the pressure to pore throat relationship assuming the pores are cylindrical (Washburn, 1921).

Equation 3.1 describes the Washburn Equation for pressure to pore throat relationship.

$$\Delta P = -\left(\frac{2\gamma\cos\theta}{r}\right) \dots\dots\dots(3.1)$$

Where,

ΔP – Difference in pressure across the curved mercury interface (psia);

γ – Surface tension for mercury (dynes/cm);

θ – Contact angle between the porous medium and mercury (degrees);

r – Corresponding pore throat radius (μm).

Prior to the Wang et al. (2016) paper, this equation assumed a constant value for both contact angle and surface tension. Wang's recent work suggests varying values for contact angle and surface tension when the pore throat diameter is less than five nanometers. This requires the necessary modification of contact angle and surface tension values relative to r, as pore throat size diminishes. In their paper, Wang et al.

(2016) explains the intricacies of calculating new values for contact angle and surface tension resulting in the new modified Washburn equation displayed below (Equation 3.2).

$$\Delta P = -\left(\frac{2\gamma_{Hg}(r) \cdot \cos\theta_{Hg}(r)}{r}\right) \dots \dots \dots 3.2$$

During the test the MICP machine collects data regarding applied pressure and induced intrusion at its respective specific pressure (Gao and Hu, 2012; Hu and Ewing, 2014). The Washburn equation assumes shale pores are cylindrical; this is an unrealistic assumption in nature but provides a representation of pore distribution, which is applicable in petrophysics.

The MICP approach can also derive permeability indirectly. This can be done mathematically using the Katz and Thompson (1986; 1987) equation. We use Equation 3.3. to calculate permeability using the applied pressure and intrusion volume measurements from the MICP data.

$$k = \left(\frac{1}{89}\right) (L_{max})^2 \left(\frac{L_{max}}{L_c}\right) \Phi S(L_{max}) \dots \dots \dots (3.3)$$

Where,

k – Sample permeability to air (μm);

L_{max} – Pore-throat diameter when hydraulic conductance is at a maximum (μm), when mercury starts to percolate through the whole sample;

L_c– Length of pore throat diameter (μm) corresponding to threshold pressure (taken from inflection point on intrusion curve) (psia);

Φ – Porosity of the sample (%);

S(L_{max})– Mercury saturation at percolation (L_{max}) (Gao and Hu, 2012).

Tortuosity aids in the understanding of fluid migration through pore matrices. Using direct MICP measurements, tortuosity can be empirically determined using

Equation 3.4 (Hager, 1998; Webb, 2001). Tortuosity can also be related to effective diffusion coefficient and travel distance of molecules (Hu et al, 2015a).

$$\tau = \sqrt{\frac{p}{24k(1+pV_{tot})} \int_{\eta=r_c, min}^{\eta=r_c, max} n^2 f_v(n) dn} \dots \dots \dots (3.4)$$

Where,

τ – Tortuosity;

P – Density of mercury ($\frac{g}{cm^3}$);

V_{tot} – Total pore volume ($\frac{ml}{g}$);

$\int_{\eta=r_c, min}^{\eta=r_c, max} n^2 f_v(n) dn$ – Pore throat volume distribution by pore-throat size.

Procedure for MICP Tests

Before MICP analysis, the shale samples are oven-dried at 60°C for 48 hours to remove moisture. Immediately after being taken out they are cooled to room temperature (~23°C) in a desiccator with less than 10% relative humidity. Once sample has completely cooled it is placed into a penetrometer. A penetrometer is an apparatus consisting of a sample chamber connected to a metal precision-bore and glass capillary system. The sample is then properly sealed and placed into a low-pressure chamber where it is evacuated to 6.7 Pa (0.05 torr, 0.000972 psi, 50 μm Hg, or 99.993% vacuum) in order to remove air and moisture. After evacuation, the sample undergoes low-pressure intrusion, which involves filling the penetrometer with mercury to a pressure of 30 psia (0.21 MPa). As the mercury invades the sample, it overcomes the capillary pressure of the pore throats, which average a diameter of 50 μm (dependent upon the choice of the penetrometer). Equilibrium time is then given in order for the mercury to

stabilize within the sample before the next pressure is applied (Chukwuma, 2015); the equilibrium time during the low-pressure testing is set to 10 seconds for shale samples.

In high-pressure testing, the pressure is increased in steps from 30 psia up to 61,000 psia (420 MPa) with an equilibrium time of 45 seconds for each step. During each step the mercury volume intruded is monitored at a detection limit of $< 0.1 \mu\text{L}$. At its highest pressure, mercury can invade pore throats as small as 2.8 nm. Permeability and tortuosity can be calculated using the physical properties of mercury (interfacial tension), the contact angle between mercury and the sample, pore throat radii, and porosity (Gao and Hu, 2012; Hu and Ewing, 2014). One important discrepancy of MICP analyses is the underestimation of larger pores and the over estimation of smaller pores. This phenomenon is called the ink-bottle effect (e.g., Chukwuma, 2015). This effect refers to the smaller pore throats connected to larger pores within the sample. By having to reach a high pressure in order to pass through this initial small pore throat, the data reflects a larger amount of small pore throat diameters than really exist (Hu and Ewing, 2014).

3-4 Pyrolysis and XRD

Pyrolysis and XRD analyses were performed on samples from wells Rogers #3804 and Wright 44#1E. Well reports were organized and performed by SCAL Laboratories in Midland, Texas. Geochemical analyses were unable to be completed on site so they were sent off to Weatherford Laboratories. The methods and procedures from Weatherford Laboratories are attached in Appendix A. XRD was performed by SCAL Laboratories; they were unable to be reached resulting in no specific laboratory methods and procedures for their XRD experimentation. Weatherford Laboratories offered their methods and procedures for XRD analyses for general understanding of such experimentation in Appendix B.

3-5 Production Data

Drilling Info gathers production data on a monthly basis from the Texas Railroad Commission. By a complimentary subscription of Drilling Info provided to the Dr. Qinhong Hu's research group here at the University of Texas at Arlington, production data can be viewed quickly and accurately.

Chapter 4

Results










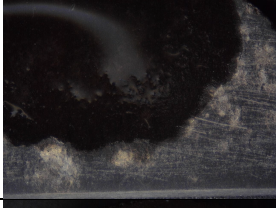




4-1 Wettability


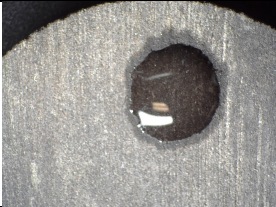




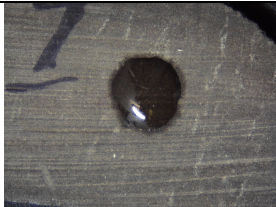
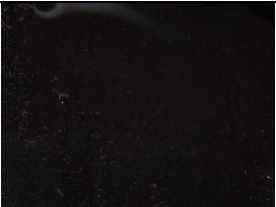






Wettability test values are presented in Table 4-1 and test pictures in Table 4-2. Distilled water and API brine fluids were tested on all 12 samples. IPA and n-decane tests were performed on 8 samples. For DI water on the 1-10 scale, every sample fell into the one to two range, indicating non-water wetting characteristics of the samples. In further support of this, every sample tested with the oil-wetting n-decane fluid showed a measurement value of 9 or 10, being nearly completely spread onto the rock. With IPA being a Zwietering fluid, a low mixture of IPA and DI water, (1% IPA fluid) showed measurements leaning towards the water wetting side with values between two and four. API brine showed larger values falling between four and six. Sample numbers three and six displayed the lowest of the brine values with a rating of three. These high brine values support why brine water is most commonly used as a hydraulic fracturing fluid.

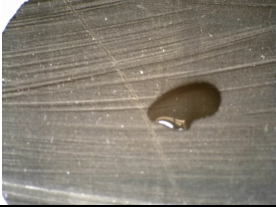


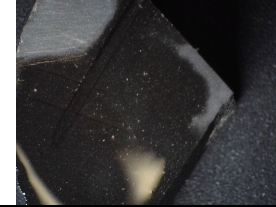

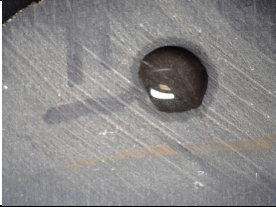
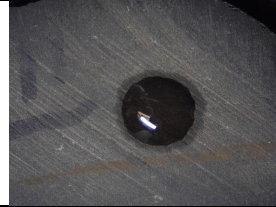





Table 4-1 Wettability Results

Sample ID	Wettability drop (2 μ L) test description			
	DI	API brine	1% IPA 99% DI	n-decane
Spra1	1	5	4	10
Spra2	1	5	-	-
Spra3	2	3	4	9
Spra4	2	6	2	9
Wolf1	2	4	-	-
Wolf2	2	3	-	-
Wolf3	2	4	3	10
Wolf4	2	6	4	10
Wolf5	2	4	-	-
Wolf6	1	4	2	10
Wolf7	1	5	4	10
Wolf8	2	6	4	9

Table 4-2 Wettability Test Pictures

Sample	DI Water	API Brine	1% IPA	N-decane
Spra1				
Spra2			TEST NOT PERFORMED	TEST NOT PERFORMED
Spra3				
Spra4				

Wolf1			TEST NOT PERFORMED	TEST NOT PERFORMED
Wolf2			TEST NOT PERFORMED	TEST NOT PERFORMED
Wolf3				
Wolf4				
Wolf5			TEST NOT PERFORMED	TEST NOT PERFORMED

Wolf8										
Wolf7										
Wolf6										

4-2 Mercury Intrusion Capillary Pressure

MICP analysis is able to produce copious amounts of information about pore structure, both directly and indirectly. Table 4-3 displays all values determined from MICP analysis. As mentioned earlier in the methods section, samples Spr1, Spr3, Wolf3, and Wolf7 were unable to be analyzed via the MICP method due to their lack of size. In order for the MICP analyses to record reliable data, the ideal sample mass should lie between 1.5 and 3 grams for shale samples with the appropriate penetrometer.

Total pore area showed a relatively wide range with values between 1-9 m²/g, with a general trend of becoming less the deeper the samples were taken within the well bore. Reliably enough, porosity values in terms of percentage show the exact same trend starting out at 9% in Spr2 and diminishing down to .87% in Wolf6, although Wolf8 does rise back up to 2%. The shallower samples in the Wolfcamp formation show relatively larger median pore throat diameter values, with the greatest values occurring between samples four and six. Bulk density and apparent skeletal density do not vary much, values occur between 2.3 and 2.6 g/cm³. The highest values occur in samples Wolf5 and 6, showing values of ~ 2.6 g/cm³. All samples but one (Wolf1) contain pores with throats less than 3 nanometers. This is determined by whether or not intrusion occurs at the very highest pressures during the experiment (~ 61,000 psi). These very small pores will also be discussed during the viewing of the pore throat distribution data.

Throughout the MICP procedure, inflection points are chosen depending on a spike in intrusion volume. These spikes represent moments of rapid intrusion into pore throats when the pressure has surpassed the capillary pressure of a specific pore size. Intrusion within specific pressure ranges have been determined by rock mechanic experiments. Figure 4-1 displays an example of these inflection points from processed MICP data.

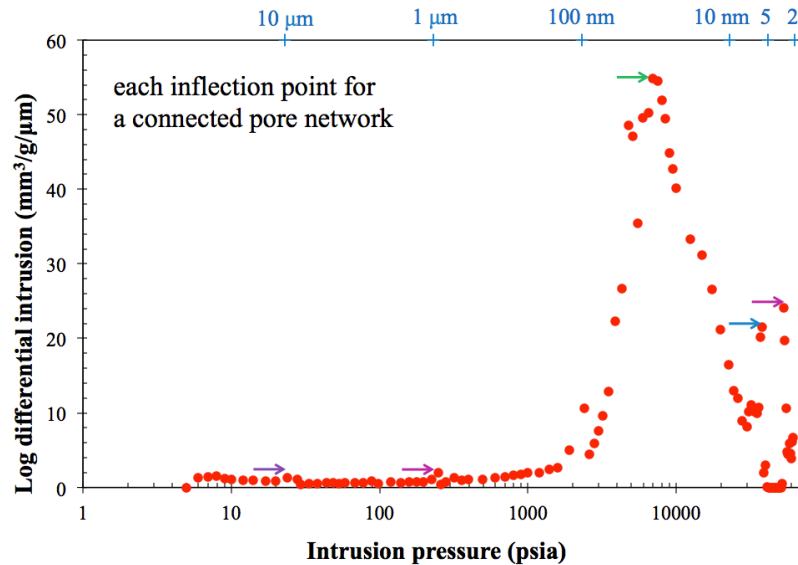


Figure 4-1 Example of Chosen Inflection Points (Sample-Spra2)

Permeability is displayed in two different formats, geometric and harmonic. Geometric is more relatable to core plug analyses while harmonic favors the smaller values in consideration of tortuosity. Both types of values occur within the nano-darcy (nD) scale. At the shallowest depths, the geometric permeability values are relatively high in the hundreds of nD region, with a general trend of lowering to the tens of nD range. Harmonic permeability decreases with depth except at the shallowest depths where they begin to rise. This rise of only 3 nD can be considered as negligible. Sample Wolf6 displays a relative regional high in geometric permeability with a value of 95 nD, which is not seen in harmonic permeability.

As discussed in the methods section, tortuosity is the quantification of how complicated the pathway is for fluid to travel through a porous medium. In Table 4-3 two types of tortuosity values are listed: matrix tortuosity involves the normal use of the tortuosity equation and geometric tortuosity factors in the porosity of the rock (Hu et al., 2015a). Variability is relatively large in matrix tortuosity spanning between 1300 and 4500

(dimensionless). Largest tortuosity values can be seen in samples Wolf5 and 6. On the other hand, geometric tortuosity starts off the largest at the shallowest of depths with a value of 14.08 and generally decreases as the samples become deeper.

Using pressure inflection points identified during the intrusion process, and the modified Washburn equation, pore throat range distributions can be determined for the sample in question. Figures 4-2 and 4-3 show pore throat size distribution against the amount of pore volume percentage each specific range accounts for. Figure 4-2 shows results for MICP samples Spr2 and Spr4 and Figure 4-3 shows samples Wolf1-8.

These different range sizes can be associated with different pore types of shale;

- 50-1 micrometer range is related to micro fractures within the rock
- 1-.05 micrometers being intergranular pore space
- 50-10 nanometers being intragranular pore space
- 10-5 nanometer sized pores have recently been interpreted as pore space created predominantly by organic matter (Lohr et al., 2015)
- 5-2.8 nanometers are believed to be under such pressure they are beginning to intrude into the space between clay grains (intraclay) (King et al., 2015)

The more shallow samples in Figure 4-2 show a more dominant presence in ranges around 10-100 nanometers. The deeper samples in Figure 4-3 show a strong presence in the 50 nm and less ranges. This is interesting as the more shallow samples are Spraberry and the deeper are Wolfcamp.

Table 4-3 MICP Results

Sample ID	Depth (ft)	Sample Mass Used (g)	Total pore area (m ² /g)	Median pore-throat diameter D ₅₀ (Volume) (nm)	Median pore-throat diameter (Area) (nm)	Bulk density (g/cm ³)	Apparent (skeletal) density (g/cm ³)	Porosity (%)	Pores less than 3 nm (yes/no)	Geometric Permeability (nD)	Harmonic Permeability (nD)	Matrix Tortuosity	Geometric Tortuosity L _c /L
Spra1	7,503												
Spra2	7,505	1.62	9.69	23.90	11.50	2.29	2.51	9.04	Yes	191.70	41.15	2261	14.08
Spra3	7,514												
Spra4	7,517	2.14	4.96	62.30	16.40	2.32	2.53	8.60	Yes	176.00	72.09	1393	10.91
Wolf1	7,665	1.63	2.17	16.80	77.00	2.48	2.53	1.92	No	411.30	28.17	2719	6.67
Wolf2	7,744	1.47	5.32	9.00	4.30	2.43	2.50	2.67	Yes	72.63	3.45	3430	9.56
Wolf3	7,787												
Wolf4	7,791	2.03	8.62	6.20	4.20	2.48	2.57	3.48	Yes	15.81	4.13	2391	8.78
Wolf5	7,808	2.46	2.03	7.20	4.00	2.61	2.63	1.03	Yes	19.72	1.15	3967	5.89
Wolf6	7,816	2.16	1.51	18.00	4.20	2.59	2.61	0.87	Yes	95.41	1.49	4525	6.15
Wolf7	7,820												
Wolf8	7,856	1.90	7.05	5.90	4.30	2.43	2.50	2.71	Yes	10.22	3.01	2444	6.26

*All sample dimensions are chip fragments (largest linear length to percolate <5 mm)

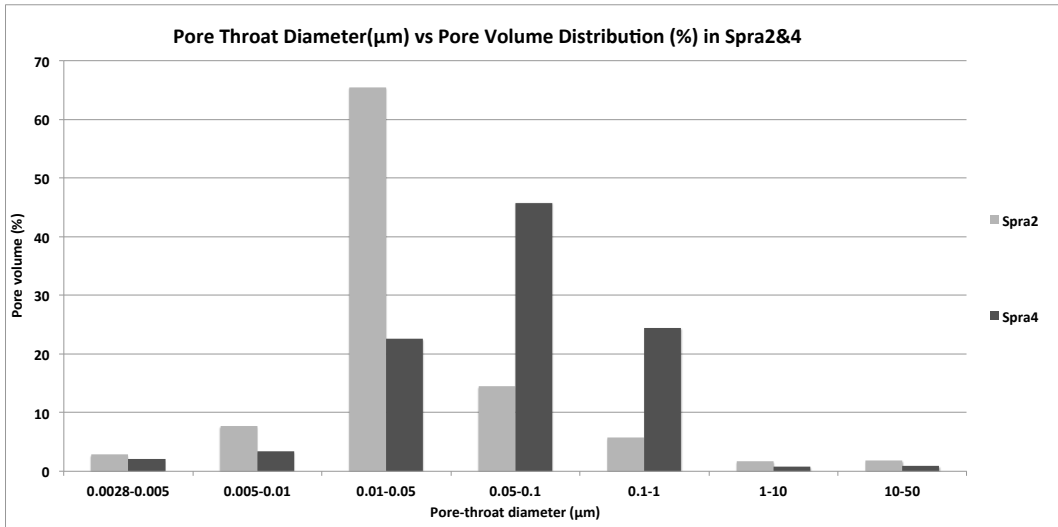


Figure 4-2 Pore Throat Diameter vs. Pore Throat Distribution in Spra2&4 (Lower Spraberry)

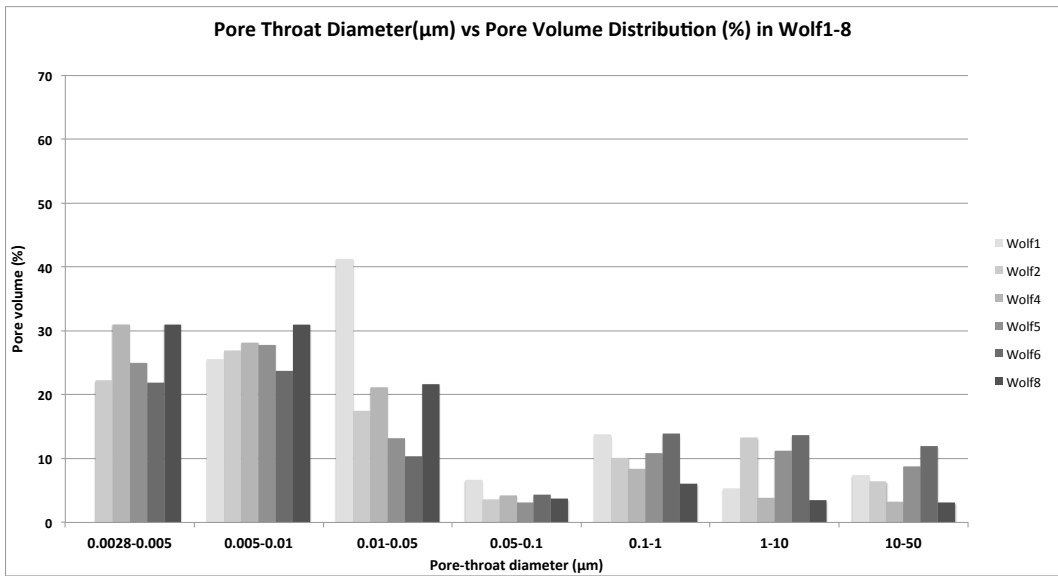


Figure 4-3 Pore Throat Diameter vs. Pore Throat Distribution in Wolf1-8 (Wolfcamp Formation)

4-3 Mineralogy

X-ray diffraction was performed for all 12 samples in the Rogers #3804E well and a total of 16 samples in the Wright 44#1E well Figures 4-4 and 4-5. Mid way through their sample interval both wells show large amounts of carbonate content, some even making up to 50% of the composition. At the most shallow and deepest regions, composition is dominated by quartz and clay material, with little to no carbonates. Salts and metallic minerals have weight percentages which can be regarded as negligible for our purposes.

Figure 4-6 is a ternary diagram created by Schlumberger (2014) for categorizing lithofacies of organic mudrock samples. They have included it in many of their recent brochures comparing shale samples from different regions. Both the Rogers and Wright samples have been plotted on this diagram for comparison. Both wells show a large percentage of samples which plot within what are classified as clay-rich siliceous mudstone. Most samples outside of this clay-rich siliceous zone plot just towards the carbonate corner of the graph within the argillaceous/siliceous mudstone, mixed siliceous mudstone, and mixed mudstone areas. There are two samples which plot within the mixed carbonate mudstone area, Rogers Sample Wolf6 and Wright Sample #7.

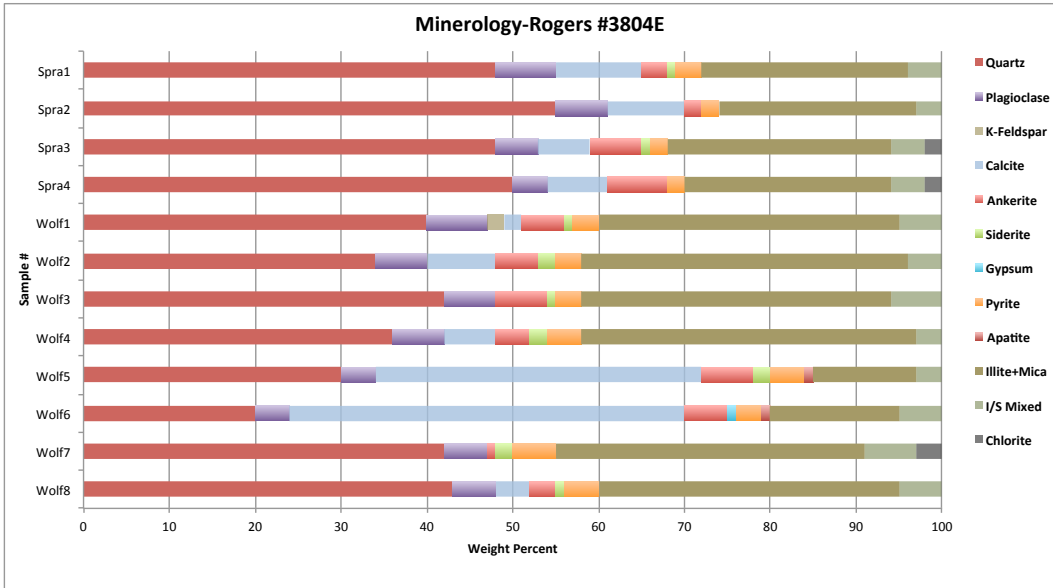


Figure 4-4 Minerology of Rogers #3804 Well in Weight Percent

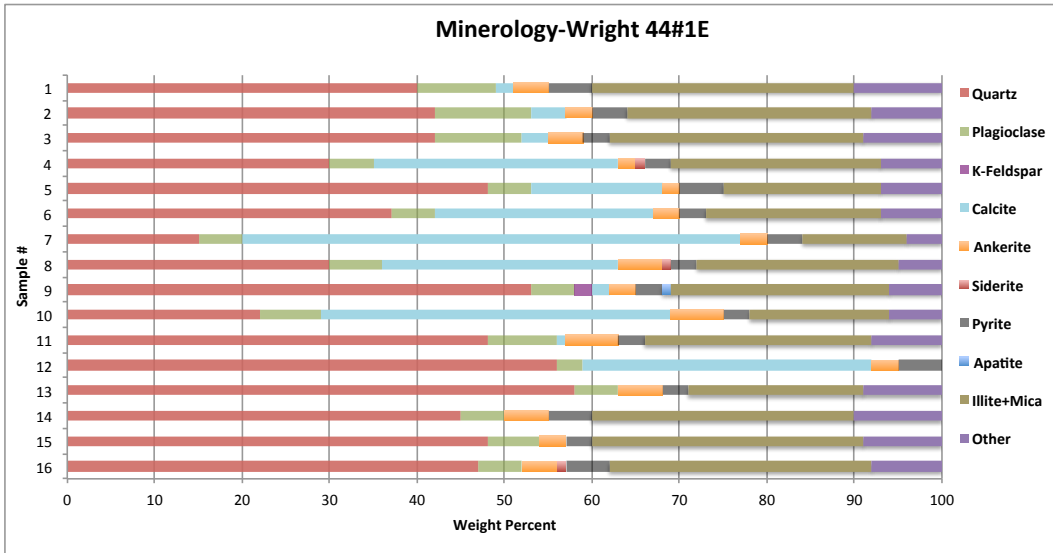


Figure 4-5 Minerology of Wright 44 #1E Well in Weight Percent

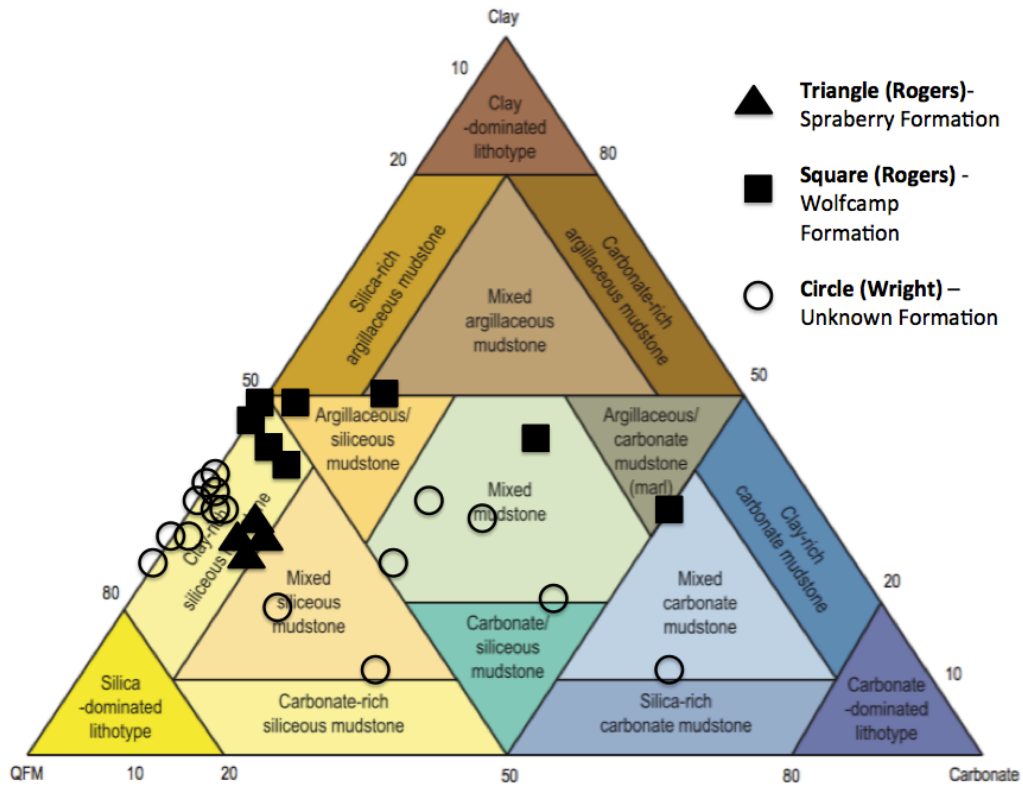


Figure 4-6 Samples from both Rogers #3804E and Wright 44#1E Plotted on a Ternary Diagram for sCore Lithofacies Classification Scheme for Organic Mudstones Proposed by Schlumberger (2014). Spraberry: triangle, Wolfcamp: square. Sample Formations not known for Wright. (filled for Roger, open for Wright).

4-4 Pyrolysis

Geochemical data from wells Rogers #3804E and Wright 44#1E are listed in Table 4-4. Vitrinite reflectance was not provided for either well but most other relevant geochemical properties are. Of particular interest for this study are total organic carbon (TOC), Tmax, kerogen type, and S1 values. S1 is the mass of currently present hydrocarbons per mass of rock (mg/g). S2 is the measurement of total hydrocarbons left immature within amount of rock (mg/g). Tmax is the highest temperature, in Celsius, reached to achieve maximum S2 yield. Tmax values for every sample lie between 430-450 degrees Celsius, well within the mature range. TOC values range from 1.5% to almost 5%, with high and low values occurring at both shallow and deep locations. S1 values occur within 1-4 mg of free liquid hydrocarbons per gram of rock with the exception of four samples; all of these higher values occur at the most shallow depths within the sampled range and are within the Spraberry Formation (Figure 4-7). Daniel Jarvie (2012) displays a generation index based on the comparison of TOC and S1. In his research he points out formations are more prone to produce hydrocarbons during hydraulic fracturing if they “crossover”, or occur above this generation index (Jarvie, 2012). Figure 4-8 shows S1 vs. TOC of Rogers 3804 and Wright 44 wells with reference to Jarvie’s crossover line.

Table 4-4 Geochemical data of both Rogers #3804 and Wright #44 Wells

Sample ID	Well	Depth	Kerogen Type	TOC (%)	S1 (mg/g)	S2 (mg/g)	S3 (mg/g)	Tmax (C°)	HI	OI	PI
Spra-1	Rogers 3804	7,503	2	3.98	6.06	14.81	0.69	439	373	17.4	0.29
Spra-2	Rogers 3804	7,505	2	3.66	7.01	13.68	0.68	442	374	18.6	0.34
Spra-3	Rogers 3804	7,514	2	3.34	4.74	11.08	0.75	449	332	22.5	0.30
Spra-4	Rogers 3804	7,517	2	2.71	5.48	9.50	0.86	442	351	31.7	0.37
Wolf-1	Rogers 3804	7,665	2	2.35	2.32	6.59	0.61	449	281	26.0	0.26
Wolf-2	Rogers 3804	7,744	2	3.94	2.98	11.41	0.66	447	290	16.8	0.21
Wolf-3	Rogers 3804	7,787	2	2.55	3.27	7.95	0.68	439	312	26.7	0.29
Wolf-4	Rogers 3804	7,791	2	2.71	3.26	8.20	0.60	444	303	22.1	0.28
Wolf-5	Rogers 3804	7,808	2	2.34	2.60	6.74	0.66	443	289	28.3	0.28
Wolf-6	Rogers 3804	7,816	2	1.93	1.86	4.53	0.63	451	235	32.7	0.29
Wolf-7	Rogers 3804	7,820	2	3.97	3.51	12.15	0.68	449	306	17.2	0.22
Wolf-8	Rogers 3804	7,856	2	3.66	3.76	11.07	0.60	444	303	16.4	0.25
1	Wright 44E	7,642	2-3	2.24	1.73	7.50	0.62	441	335	28.0	0.19
2	Wright 44E	7,767	2-3	2.68	1.94	5.98	0.63	448	223	23.0	0.24
3	Wright 44E	7,887	2-3	1.89	1.36	4.15	0.53	445	220	28.0	0.25
4	Wright 44E	8,036	2-3	3.08	1.86	9.07	0.75	448	295	24.0	0.17
5	Wright 44E	8,057	2-3	2.4	1.25	4.64	0.64	443	193	27.0	0.21
6	Wright 44E	8,092	2-3	3.48	3.13	11.93	0.59	447	343	17.0	0.21
7	Wright 44E	8,100	2-3	2.14	1.59	4.61	0.61	445	216	29.0	0.26
8	Wright 44E	8,131	2-3	2.49	1.89	7.42	0.73	445	298	29.0	0.20
9	Wright 44E	8,173	2-3	2.88	2.49	5.97	0.71	445	207	25.0	0.29
10	Wright 44E	8,186	2-3	2.59	2.12	5.44	0.73	450	210	28.0	0.28
11	Wright 44E	8,212	2-3	2.65	2.57	5.34	0.74	444	201	28.0	0.32
12	Wright 44E	8,222	2-3	1.52	1.21	2.31	0.64	446	152	42.0	0.34
13	Wright 44E	8,300	2-3	1.83	2.75	3.44	0.72	441	188	39.0	0.44
14	Wright 44E	8,309	2-3	1.53	1.48	1.89	0.69	442	124	45.0	0.44
15	Wright 44E	8,339	2-3	2.92	2.46	7.31	0.68	446	250	23.0	0.25
16	Wright 44E	8,341	2-3	4.63	3.17	11.73	0.73	448	253	16.0	0.21

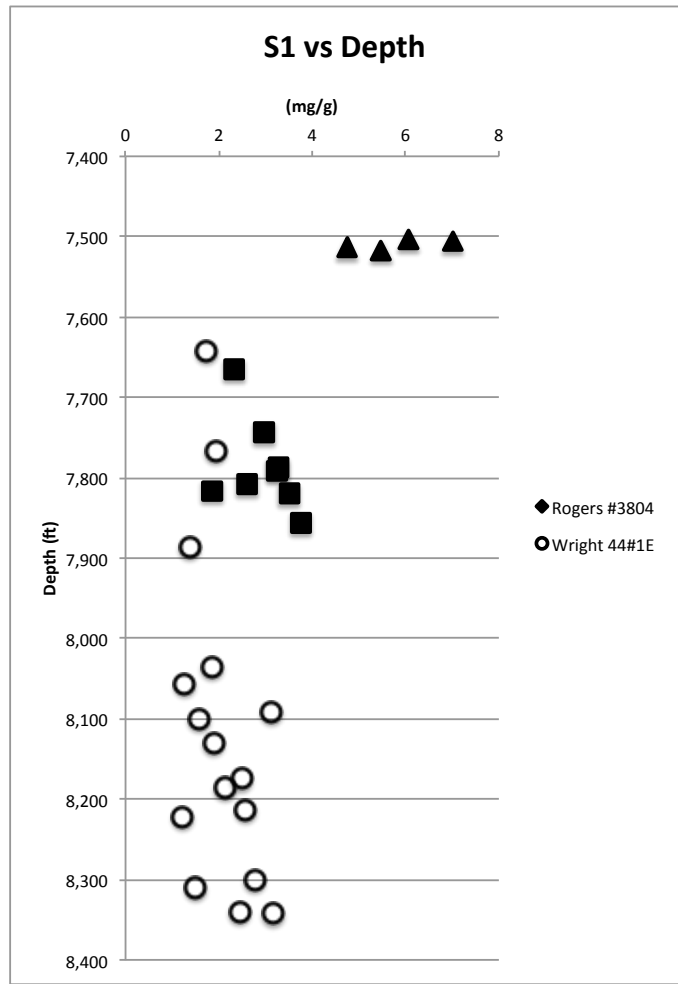


Figure 4-7 S1 vs. Depth in Rogers #3804E and Wright 44#1E Wells

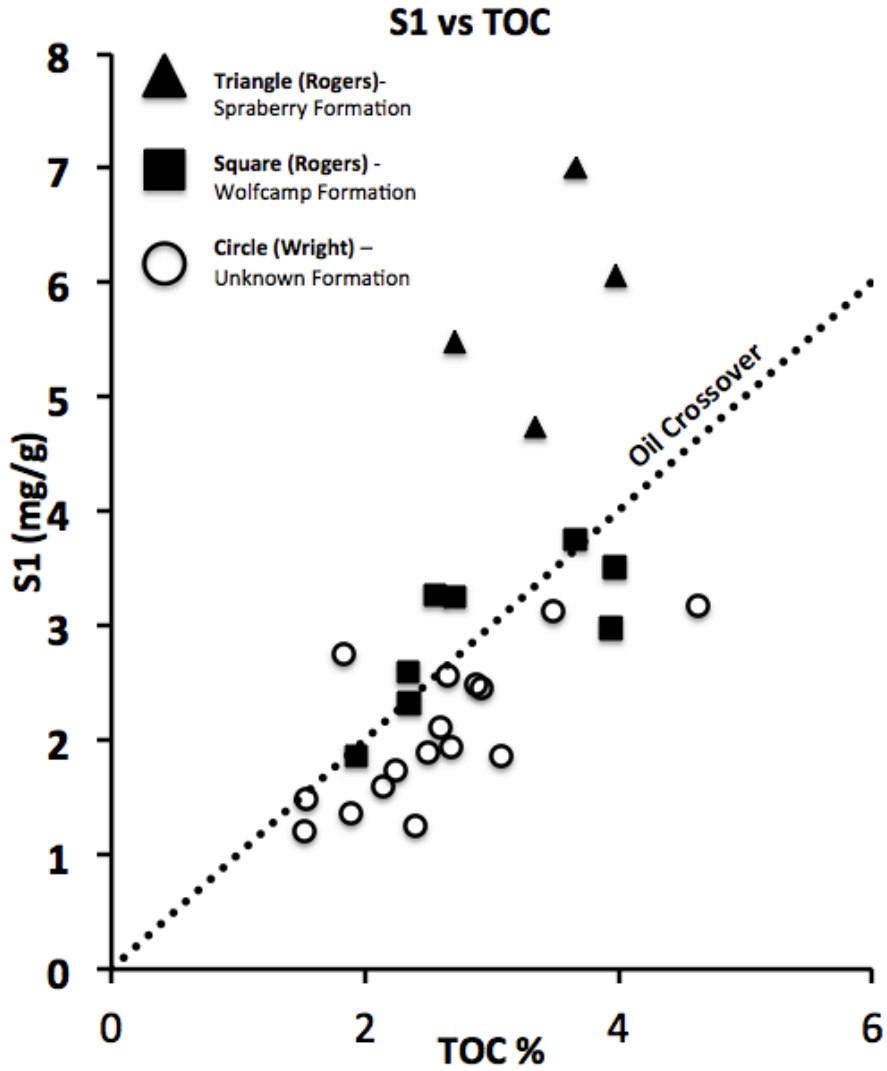


Figure 4-8 S1 vs. TOC with reference to Jarvie's Crossover Generation Index in Rogers

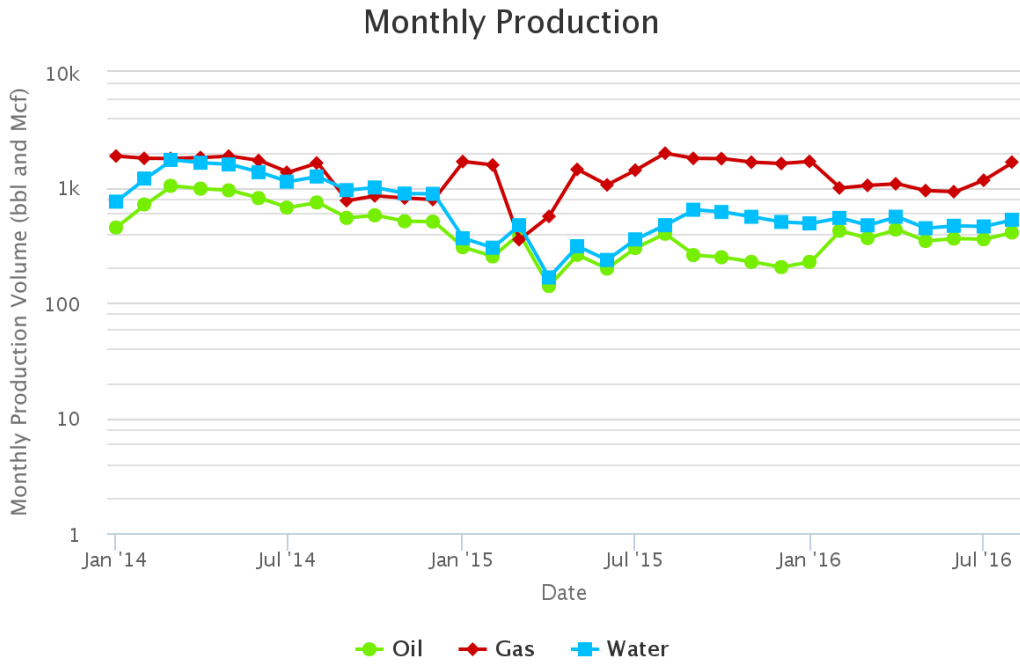
#3804E and Wright 44#1E Wells

4-5 Production

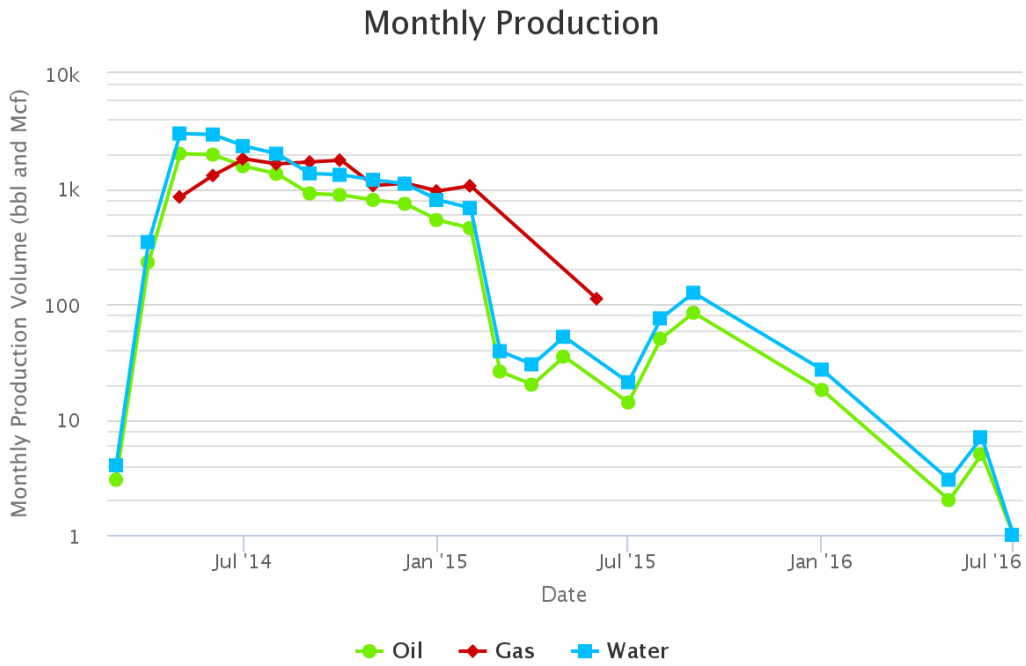
Rogers #3804E, Wright #44E, and Garrett-Reed 37-48 wells all have production data in Drilling Info going back to their initial production in 2014. The intricacies of their production behavior will not be discussed in this paper. The general trend of their production history will be compared to the geochemical and petrophysical properties discussed in this paper. Rogers #3804 and Wright #44 start off initially producing approximately 1000 bbl and mcf per month. As time progresses Rogers stays with a nearly consistent production, while Wright declines eventually to approximately zero production within the matter of 26 months. As seen in Table 4-5 the perforation interval for the Wright well is less than half of the Rogers well. This could effect overall production compared to the Rogers well but the dramatic production decline can be explained by petrophysical and geochemical characterization like in Figure 4-8. The Garrett-Reed well starts off much higher around 10,000 bbl/mcf while staying consistent to August 2016.

Table 4-5 Well information for Three Wells

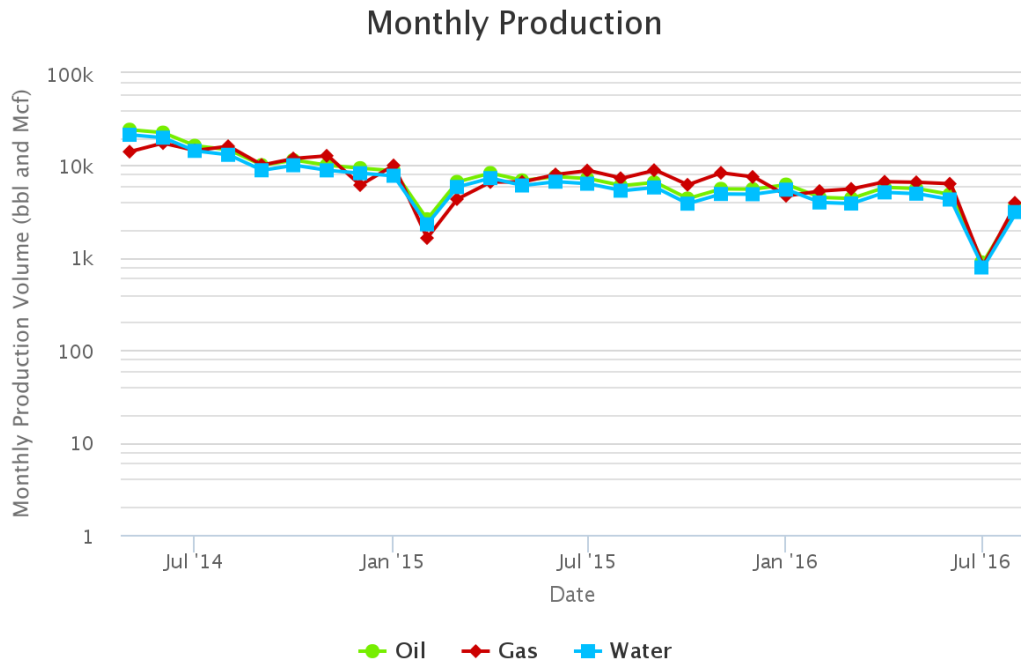
	Rogers #3804	Wright 44 #1E	Garrett-Reed 37-48
Completion Depth (ft)	9961	8700	TVD:7817, TMD:15490
Horizontal/Vertical?	Vertical	Vertical	Horizontal
Stimulation Depth and Interval (Perferation)(ft)	7400-9661 ft (2263 ft)	7638-8550 ft (912 ft)	8080-14125 ft (6045 ft)
Field	Spraberry (Strawn)	Spraberry (Strawn)	Spraberry Trend



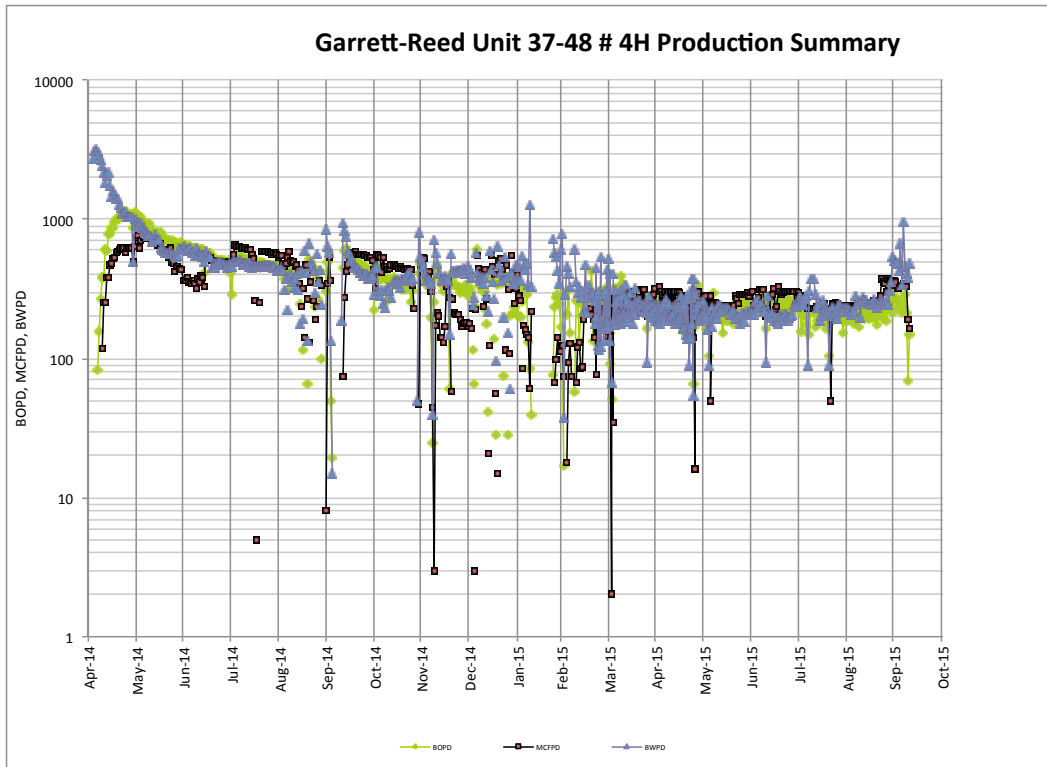
(A) Rogers #3804E



(B) Wright #44E



(C) Garrett-Reed 37-48



(D) Garrett-Reed 37-48 (Daily Production)

Figure 4-9 Monthly Production Data: (A) Rogers #3804E; (B) Wright #44E; (C) Garrett-Reed 37-48; (D) Garrett-Reed 37-48 (Daily Production). (Drilling Info, 2016).

Chapter 5

Discussion and Conclusions

Wettability, mercury intrusion capillary pressure, XRD, and pyrolysis experiments were performed on two different wells (Rogers #3804E and Wright 44#1E) in order to compare their petrophysical and geochemical properties. Production data of these two wells, along with another nearby well (Garrett-Reed 37-48), were provided to allow for correlation with laboratory data. Wettability and MICP were performed in the University of Texas-Arlington while XRD and pyrolysis was performed commercially at other laboratories.

5-1 Wettability

Wettability tests resulted in oil-wetting rock behavior. The high TOC content of the samples supports these values. Brine values also show the significant role salinity plays in the imbibition of fluid into mudrock, more so than 1% IPA. In some cases brine raises the extent of wetting by nearly 50% going from a wettability value of one to five.

5-2 Pore Structure vs. Mineralogy

In our mineralogy results the largest variation occurs between carbonate composition. In Figures 5-1 and 5-2 below, we show two examples within our Rogers well which both display very low carbonate content. The mineralogy is compared to their pore size distribution. These figures show very similar mineralogy properties but very different pore structure. Unfortunately, this lack of correlation between mineralogy and pore size distribution occurs throughout all of our samples. The two samples which contain the largest percentage of small organic pores are samples Wolf4 and Wolf5, which we can see in Figure 5-3, having a nearly 40% difference in carbonate content. We see this

same inconsistency with quartz and clay content in our samples. Due to these inconsistencies we must conclude while mineralogy may have some impact on pore structure within rocks of different formations, these shale samples show no correlation between mineralogy and pore size distribution.

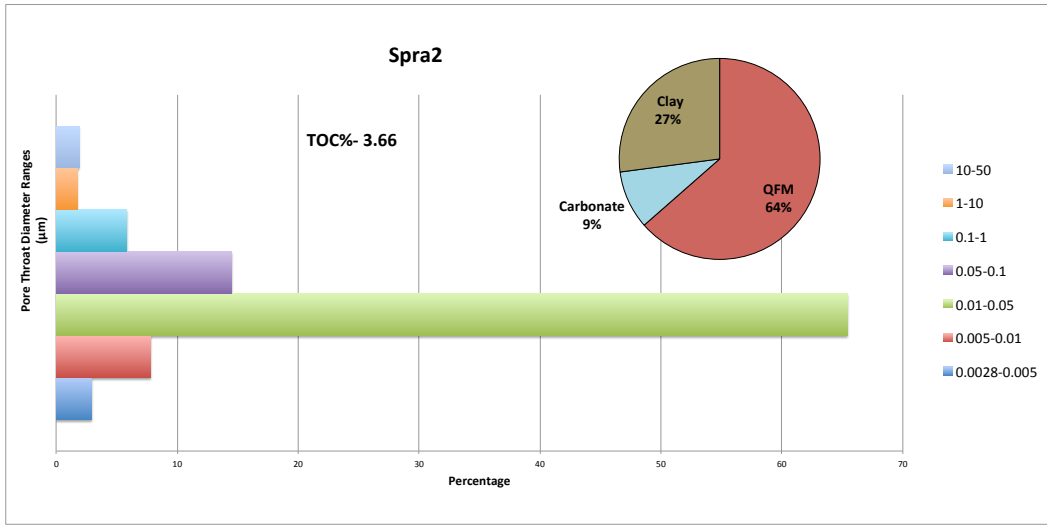


Figure 5-1 Pore Size Distribution vs. Mineralogy in Spr2

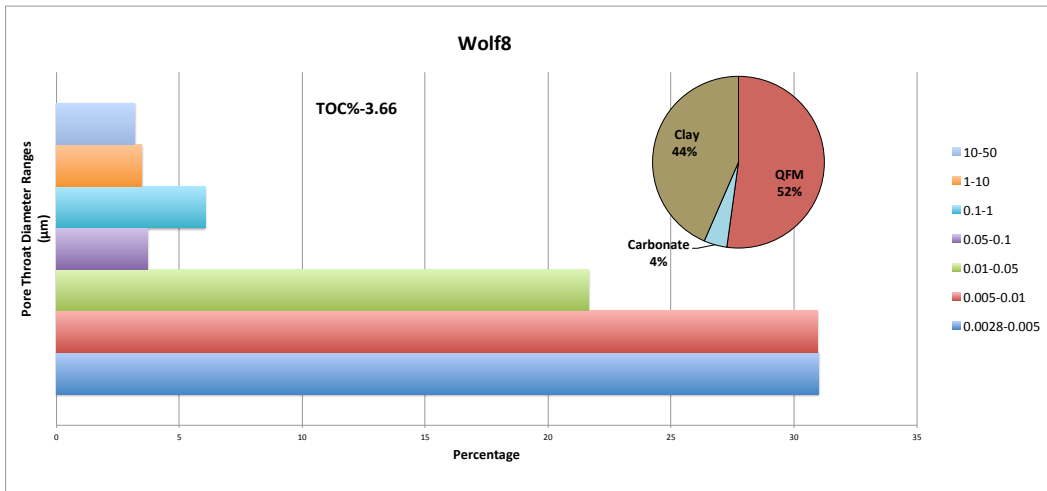


Figure 5-2 Pore Size Distribution vs. Mineralogy in Wolf8

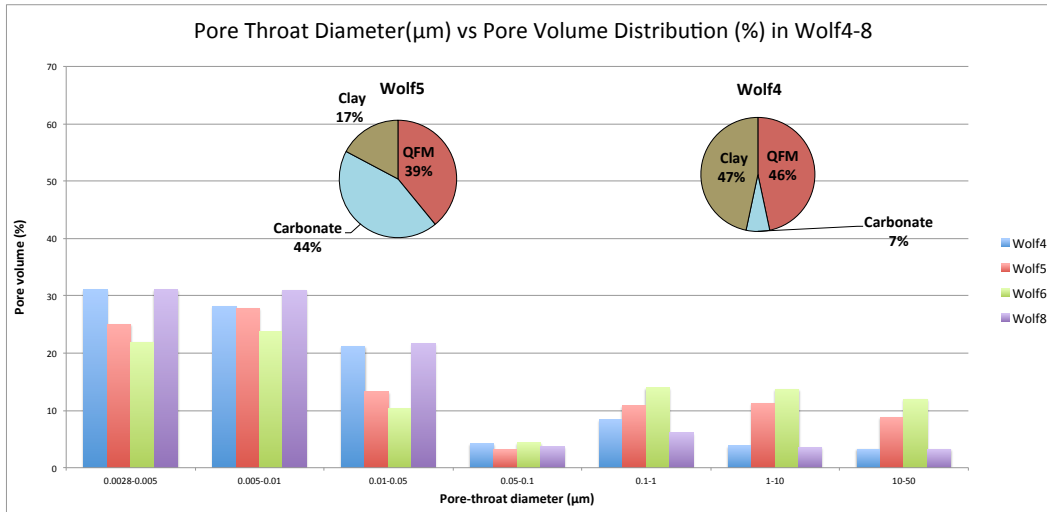


Figure 5-3 Pore Size Distribution vs. Mineralogy in Wolf 4 & 5

5-3 Organic Geochemistry vs. Mineralogy

It is generally known in petroleum geology organic rich rocks are normally shale or mudrock. While considering different compositions of mudrock we wonder whether shales show different amounts of organic content relative to different amounts of certain compositions (e.g., quartz, carbonate, or clay). Kuila et al. (2012) hypothesized that an increase of clay content brings about an increase in total organic carbon. For the Rogers and Wright wells we looked at the comparison between clay content and TOC percentage; it is noted many of the samples with clay percentages in between 20 and 40 percent were very sporadic and plotted with a wide variation TOC. Attempting to see a difference between the lowest and highest clay content within these samples, we plotted only the samples with clay content below 20% and over 40% (Figure 5-5). With this new plot we can now see a general, and somewhat subtle, trend of an increase in TOC with an increase in clay content. We are unable to determine a better correlation due to the fact we do not have a more wide variation in clay content. There was no correlation observed between TOC and other mineral compositions.

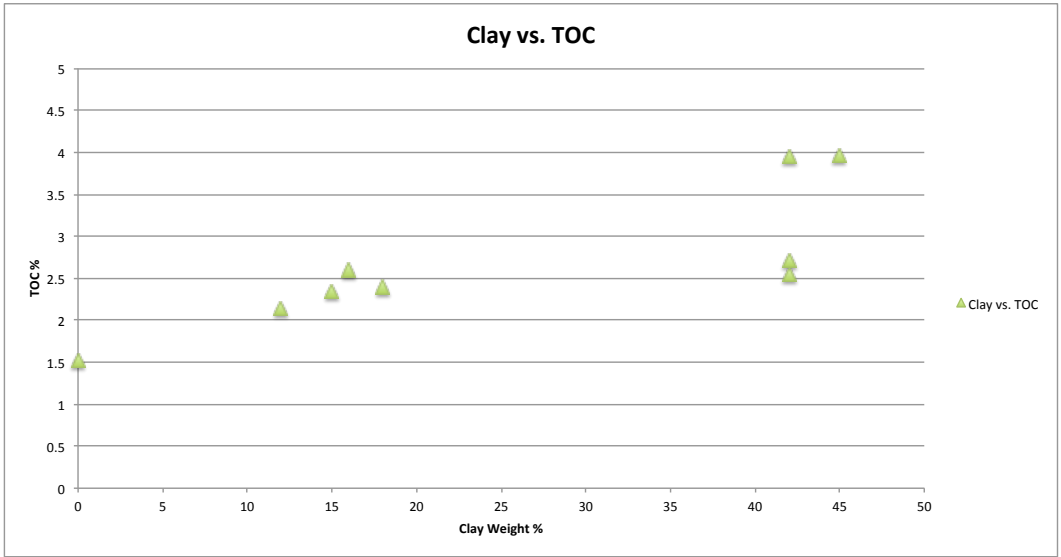


Figure 5-4 Total Organic Carbon vs. Weight Percent of Clay (Data from <20% and >40% Clay)

5-4 Pore Structure vs. Organic Geochemistry

Pore structure and thermal maturation of organic carbon present within the formation show numerous correlations with each other. S1 pyrolysis values represent the amount of hydrocarbons in milligrams per gram of rock in a measured sample. While TOC is an important factor in S1 values, thermal maturity is a more significant factor in an S1 value. Figure 5-5 compares S1 to our porosity values and we see an apparent linear correlation; when there is an increase in S1 we see an increase in porosity percentage. This implies when solid kerogen converts to hydrocarbons the resulting space is now newly converted pore space.

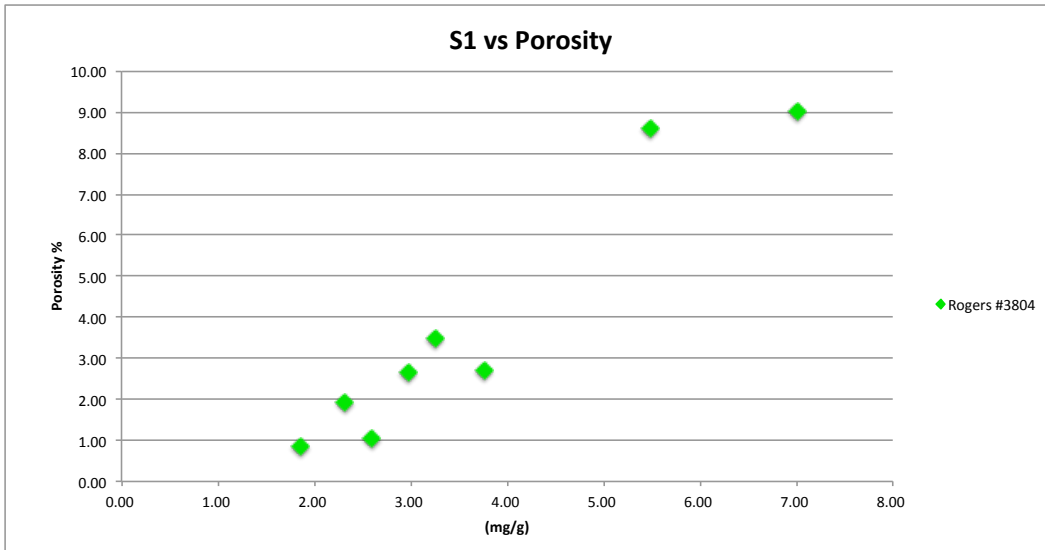


Figure 5-5 S1 vs. Porosity in Rogers #3804 Well

Combining the idea of pore development through maturation, along with the knowledge we gain from King et al. (2015) and Lohr et al. (2015) about pore size distribution, we can display whether maturation is controlling the amount of organic pores we see in our samples. Figure 5-6 shows S1 values relative to the percentage of pore-throat diameters within the 2.8-50 nm range, which are predominantly organic pores. The two values seem to act in a parallel fashion with the percentage of these organic pores mimicking the trend of the S1 values. To display the inverse of this, Figure 5-7 shows the percentage of μm -pores (1-50 μm) relative to S1 values. Sample Wolf1 seems to be a sample which does not follow the same behavior as the rest of these samples. Error could have been made during pyrolysis or MICP experimentation or perhaps this sample is just anomalous. A shaded square has been placed over the Sample Wolf1 portion of the graph for better visualization. Both of these figures support the idea of organic pore creation from maturation.

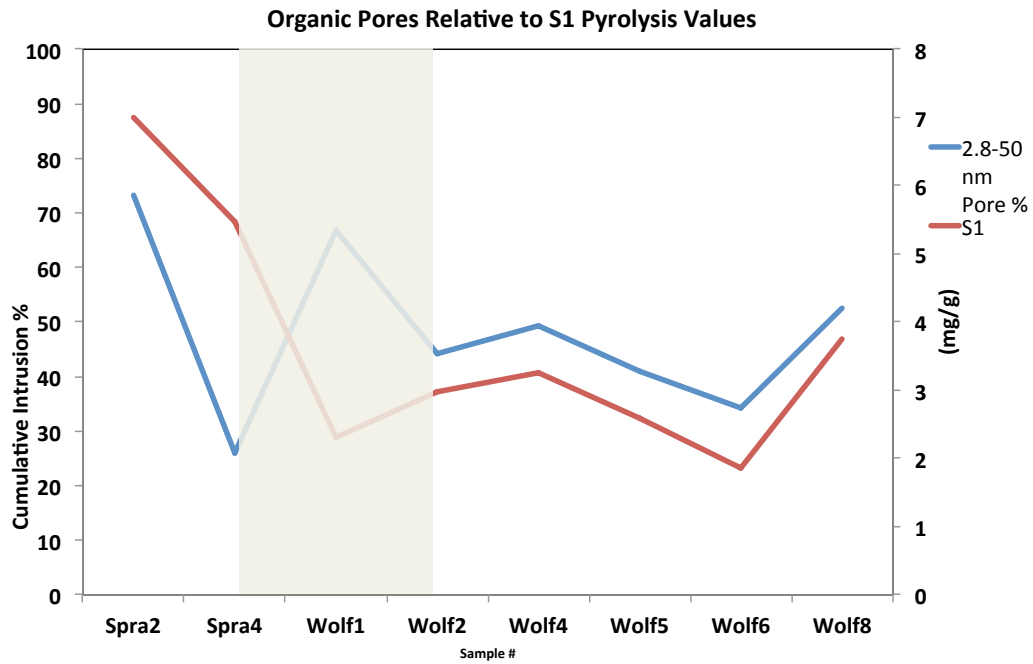


Figure 5-6 Organic Pore (2.7-50nm) Percentage relative to S1 Values

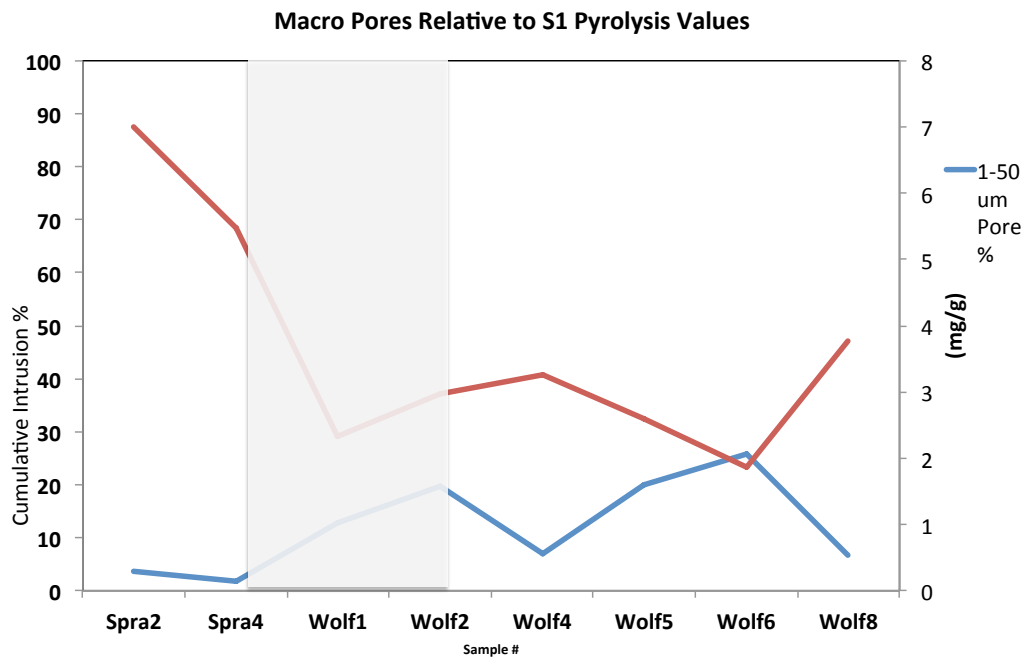


Figure 5-7 μm -Pore (1-50 μm) Percentage relative to S1 Values

King et al. (2015) also considers the presence of an interlamellar clay layer within shales. These layers are thought to be smaller than 3 nm. With the majority of hydrocarbon molecules being larger than 3 nm we should expect the percentage of these pores to not be influenced by thermal maturation of kerogen. Figure 5-8 is the exact same figure as 5-6 with the exclusion of pore sizes ranging between 2.8 and 5 nm. These two figures are nearly identical in the fact that the slopes of both sets of data are nearly parallel. This supports the idea pores smaller than ~3 nanometers are unrelated to pore creation from kerogen maturation.

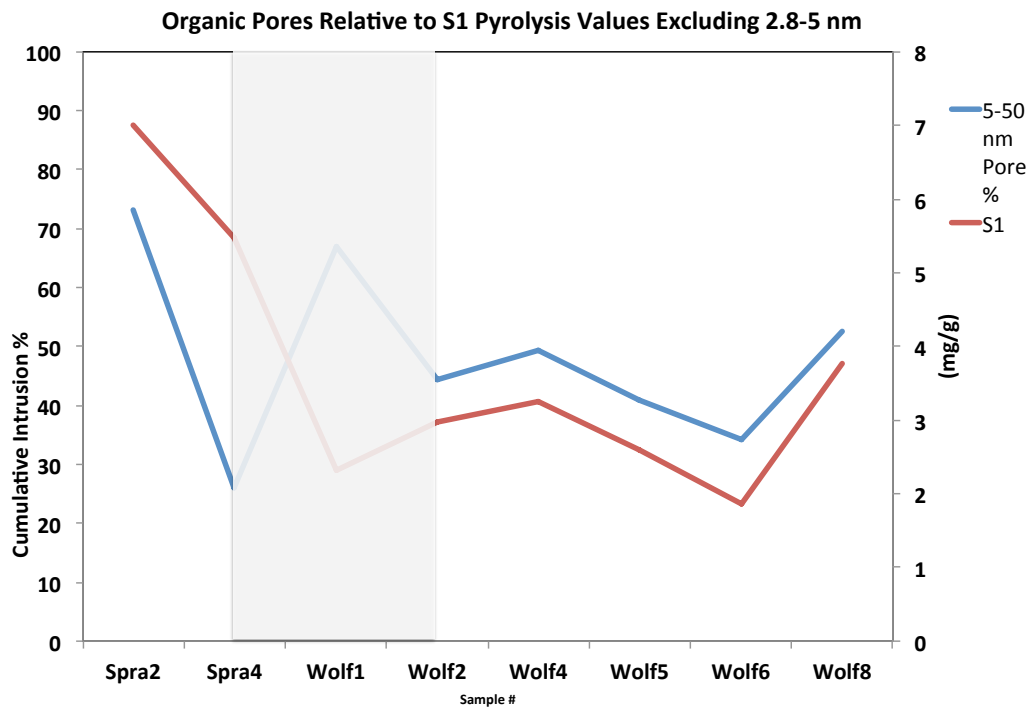


Figure 5-8 Organic Pore (5-50nm) Percentage relative to S1 Values

It is important to note that such a correlation between S1 values and the percentage of organic pores is not observed between TOC and the percentage of organic

pores. This supports the hypothesis pore creation within kerogen is not necessarily dependent on the amount of total organic carbon within the rock but rather the amount of maturation the kerogen has undergone.

5-5 Production Data

The principal difference between the Rogers #3804 well and the Wright #44 well is the significant drop in production of the Wright well. Figure 4-7 displays the comparison of S1 vs. TOC of the Rogers and Wright wells. We used Jarvie's generation index, which is used as a determinant for the producibility of a formation if the samples occur above this line, to see the majority of the Rogers samples occur above the oil crossover, while many of the Wright samples occur below. This predictor is quite consistent when compared to the production data.

The Garrett-Reed 37-48 well began producing at a much higher rate (10,000 bbl & Mcf) while maintaining a slow, consistent decline. This well is of much closer proximity (< 1 mile) to the Rogers well than the Wright well (~10 miles), so it most likely contains similar geochemical and petrophysical properties. More importantly the Garrett-Reed well is a horizontal well, which drastically alters its producibility.

5-6 Particle Size Distribution

In an attempt to explain the reasons behind the difference in petrophysical and geochemical properties between the Spraberry and Wolfcamp Formations we look to their respective particle size distributions. When incorporating Mayer and Stowe (1965) volume vs. particle size (Figure 5-9) we get a sense of the particle size distribution within the respective sample in question. We can see a distinct difference between the Spraberry and Wolfcamp samples. The Spraberry samples show a distribution of well-

sorted grains. In contrast, the Wolfcamp samples show a much wider distribution of particle sizes. Sedimentology rules explain how pore spaces are determined by the size of their grains. With the Spraberry containing similar sized grains, this would explain its larger porosity values.

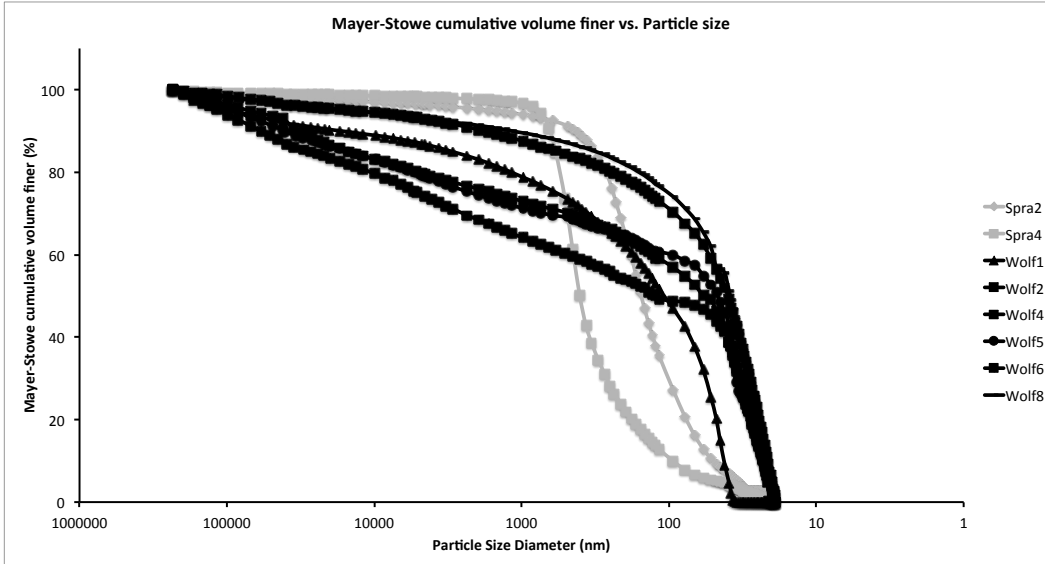


Figure 5-9 Particle Size Distribution of Rogers Samples

5-7 Conclusion

Hydrophilic (DI water, API brine) and hydrophobic (n-decane) fluids are first used to determine the wettability characteristics at the micrometer range. Mercury Intrusion Capillary Pressure is then performed to determine a wide variety of petrophysical properties at the micro- and nano-meter range, specifically pore size distribution. Organic geochemical and mineralogical properties are also determined by means of X-ray diffraction and pyrolysis analyses. S1 values were found to play the largest contribution in the determination of pore structure, showing thermal maturation and not TOC is more relevant in the production of unconventional shale plays. With an increase in S1 values

the amount of pore throat sizes between 5-50 nm increases. This 5-50 nm range can occupy over 50% of the formation pore percentage.

The “Wolfberry” trend has been produced for over six decades but this research attempts to further understand the pore structure within these formations while also understanding the factors that led to the creation of these pore systems. Historical production data is briefly compared to these formational properties to understand the reasons for the success and failure of certain wells. Jarvie’s (2012) generation index predicts the Rogers well will be more likely to produce hydrocarbons than the Wright #44 well. When we look at the historical production of the Rogers and Wright wells we see that Jarvie’s generation index is accurate.

5-8 Recommendations

A much larger data set should be gathered in order to increase the validity of these interpretations. The same exact type of study should also be conducted for Garrett-Reed 37-48 well. More research is pertinent into the behavior of the interlamellar clay layer. Samples from the same interval should also be analyzed by other experimental means (SEM, SANS, etc.) in order to further examine the particle size distribution.

Appendix A

Methods and Procedures for Geochemical Analysis at Weatherford Laboratories



Rock Sample Preparation

Samples for Total Organic Carbon (TOC) and/or Programmed Pyrolysis may each require varying levels of sample preparation. Groups of samples are evaluated as to their respective condition as received and are handled differently depending on the various types of contaminants, lithologies, and analytical objectives. Samples are not high-graded prior to grinding unless specifically instructed by the client. When necessary and as instructed, water washing may be required to remove water-based mud. Solvent washing can be utilized to remove oil-based and/or synthetic-based mud. Additional solvent extraction of the crushed rock will be necessary to completely remove the contaminating oil-based and/or synthetic-based mud. Sample picking may also be necessary to remove lost circulation material or known cavings. Samples for TOC and Programed Pyrolysis are then ground to pass through a fine mesh sieve prior to analysis.

Total Organic Carbon

Approximately 0.10 g of crushed rock is accurately weighed and then digested with concentrated hydrochloric acid to remove all carbonates from the sample. At this point, gravimetric carbonate content can be determined if requested. Following digestion, the sample is washed through a filtering apparatus, placed in a combustion crucible and dried. After drying, the sample is analyzed with a LECO Carbon Analyzer with detection limits to 0.01 weight percent. Standards and sample duplicates are tested regularly to assure superior instrument performance.

Programmed Pyrolysis (Rock-Eval II, Rock-Eval VI, Source Rock Analyzer)

Programmed pyrolysis (Rock-Eval and SRA) is performed to assess source rock quality and thermal maturity (e.g., Peters, 1986; Peters and Casa, 1994). In programmed pyrolysis, crushed rock samples are heated in an inert environment to determine the yield of hydrocarbons and CO₂. The sample is initially held isothermally at 300°C for 3 minutes, producing the S1 peak by vaporizing the free (unbound) hydrocarbons. High S1 values indicate either large amounts of kerogen-derived bitumen (as in an active source rock) or the presence of migrated hydrocarbons. The oven then increases in temperature by 25°C/minute to a final temperature of approximately 600°C, depending on the instrument type. During this time, hydrocarbons that evolve from the sample as a function of the pyrolytic degradation of the kerogen are measured, generating the S2 peak and is proportional to the amount of hydrogen-rich kerogen in the rock. The temperature at which the S2 peak reaches a maximum, "T_{max}", is a measure of the source rock maturity. Accuracy of T_{max} is 1-3°C, depending on the instrument, program rate and sample size, but can also vary by organic matter type. Tmax values for samples with S2 peaks less than 0.2 mg HC/g rock are often inaccurate and should be rejected unless a definitive kerogen peak is noted from the pyrogram. Any carbon dioxide released between 300° and 390°C is also measured, generating the S3 peak, providing an assessment of the oxygen content of the rock. In addition to the standard programmed pyrolysis method, we have several additional methods available designed to provide the client with additional useful information as it relates to the geochemical nature and potential of a rock sample including but not limited to TOC quantification, Carbonate quantification, Reservoir Oil Quality, APIR and Kerogen Kinetic analyses. A summary of analytical results from Programmed Pyrolysis follows.

- S1: free oil content (mg hydrocarbons per gram of rock)
- S2: remaining hydrocarbon potential (mg hydrocarbons per gram of rock)
- S3: organic carbon dioxide (mg CO₂ per gram of rock)
- TOC: total organic carbon content (wt. %)
- Tmax: temperature at maximum evolution of S2 hydrocarbons
- Ratios: hydrogen index (HI), oxygen index (OI), production index (PI), S2/S3, and S1/TOC

Vitrinite Reflectance and Visual Kerogen Assessment

Visual kerogen assessments complement chemical assessments by recording information from the discrete particles (macerals) that make up the sedimentary organic matter. Vitrinite macerals are particles of sedimentary organic matter derived from wood, and their reflectance of incident light under oil immersion is used to assess the thermal maturity of a sample. Vitrinite reflectance (%R_o) increases with increased depth of burial (i.e., increased thermal exposure), and is an indication of the maximum temperature to which these particles have been exposed. The reflectance microscope measures the amount of reflected light relative to the incident light and expresses this ratio as a percentage. Vitrinite reflectance values range from about 0.25% (immature) to a high of about 5 or 6% (very mature). A population of vitrinite particles is found in almost all rock samples of Devonian or younger age (older samples pre-date the evolution of land plants, the source of vitrinite). Selecting the appropriate vitrinite population for subsequent reflectance measurements is a somewhat subjective process. The *in situ* population must be identified, and must exclude vitrinite derived from cavings and reworked organic matter. Reworked vitrinite that was redeposited in the sediments may have higher reflectance that will skew the measurements towards higher R_o values if not recognized and removed from the average. In cuttings samples, cavings from overlying less mature sediments may skew the average towards lower values. Generally, when cavings are excluded, the lowest reflecting population is found to be indicative of the indigenous population, but this evaluation is made in combination with visual kerogen assessments, Rock-Eval Tmax measurements, and data for the extent of kerogen conversion.

Vitrinite reflectance values are divided into the following stages of thermal maturity:

<i>Stage</i>	<i>Reflectance Range</i>
Immature	0.2% to 0.6%
Oil window maturity	0.6% to 1.1%
Condensate or wet-gas window	1.1% to 1.4%
Dry gas window	1.40% plus

Thermal alteration indices (TAI) are determined from the color of organic matter when viewed under transmitted light through a strewn slide mount of kerogen. Lighter colored organic matter is indicative of low maturity, whereas darker material is indicative of higher thermal maturity.

Maceral composition is an assessment of the percentages of various organic particles found in kerogen samples. These particles are related to the oil and gas potential of the organic matter and are generally described as amorphous, exinitic, vitrinitic, inertinitic, or solid bitumen percentages. The former two macerals are primarily oil-prone particulate matter, whereas vitrinitic particles are indicative of gas-prone organic matter. Inertinitic matter is very hydrogen-poor and has no potential for generation of commercial quantities of hydrocarbons. The presence of solid bitumen is indicative of *in situ* generated hydrocarbons, migrated hydrocarbons, or contamination. Other observations from visual kerogen assessment include the quality of the organic matter (oxidized, well preserved), and the presence of palynomorphs (which can reveal key aspects of the depositional environment).

Appendix B

Methods and Procedures of X-Ray Diffraction Analysis at Weatherford Laboratories

Procedures for X-Ray Diffraction (XRD) Analysis

Bulk Sample Preparation

Spray Dry

A representative portion (6 grams minimum, preferably 10 grams) of each sample is selected for XRD analysis. Samples are disaggregated using mortar and pestle and portioned out for bulk and clay analyses.

The bulk portion is ground into a slurry using a McCrone Micronizing Mill. The slurry is transferred to an air brush assembly and spray dried using a James Hutton Institute Spray Drying Oven. Randomly oriented spherical aggregates are then loaded into stainless steel sample holders. This method eliminates preferred orientation of minerals and allows for improved reproducibility of the bulk XRD patterns. [Sp. Ed. Bish, D. L. and Post, J. E. (1989); Hillier, S (2002b)].

Minimal Material

A representative portion (2 grams minimum) of each sample is selected for XRD analysis. Samples are hand ground in an agate mortar and pestle to a fine powder.

A portion of each ground sample is loaded into a stainless steel sample holder, modified to accommodate a side loading method. This side loading method allows the sample to be sifted and promotes a random particle orientation, minimizing preferred orientation.

Bulk/Whole Rock Analysis

These bulk sample mounts are scanned with a Bruker AXS D4 Endeavor X-ray diffractometer using copper K-alpha radiation. To eliminate K-beta peaks and reduce background noise, nickel filter slits and air scatter screens are utilized, respectively. The scanning parameters for a bulk scan are from 5° 2θ to 70° 2θ at a step size of 0.02° per step. Full scanning parameters are defined below (for both bulk and clay):

- Operating voltage: 50Kv
- Operating amperage: 40mA
- Axial soller slit is in place

- Goniometer diameter: 400mm
- Lynx Eye High speed detector with a 2θ scanning range of 4°
- A nickel filter for K beta peaks
- An air scatter screen to reduce fluorescence
- Variable divergent slit at 0.3mm for bulk and 0.5mm for clay

Bulk Mineral Quantification

MDI Jade™ 9+ software and ICDD PDF 4+ 2015 database, with over 790,000 known compounds, are used to identify mineral phases present in the bulk diffractograms. Reference Intensity Ratio (RIR) method is used to quantify the whole rock. The RIRs (e.g., Mineral Intensity Factors (MIF)) are generated for each diffractometer using pure mineral standards mixed with quartz. The primary peaks of the minerals present are measured using the area under the curve to one standard deviation (subtracting the background). When an uncommon mineral that is not in our RIR library and pure mineral standards are not available, whole pattern fitting with Rietveld refinement is applied.

X-ray diffraction *cannot* identify non-crystalline (amorphous) material, such as organic material and volcanic glass. However, samples containing a large amount of amorphous material show an anomalous “hump” in the XRD pattern. If further evaluations are required, Bruker AXS TOPAS v4.2 software is used to provide an estimate of the amount of amorphous material. Scans undergo full-pattern-fitting and Rietveld refinement using structure phase files previously identified by Jade and ICDD software (see above).

Clay Sample Preparation

An oriented clay fraction mount is prepared for each sample from hand ground powder. The samples are treated with a small amount of sodium hexametaphosphate as a deflocculant mixed with distilled water. The samples are then physically dispersed using a Fisher Scientific Ultra Sonifier to bring the clays into suspension. The samples are sized fractionated by centrifuging. After centrifuging, the supernatant containing the less than 2 micron clay fraction is vacuumed through a filter membrane glass tube that collects the solids on to a millipore filter.

These oriented solids are mounted on glass slides producing highly uniform diffraction mounts [Drever, 1973]. The glass slides are loaded into desiccant bowls containing 99.9% ethylene glycol for an extended period of time at a temperature of 110°C. The

samples are loaded directly from the desiccant bowl to ensure maximum sample glycolation. The glycolated clays are also scanned in a Bruker AXS diffractometer using the following scan parameters: 2° 2θ to 30° 2θ at a step size of 0.02° per step.

After the glycolated slide is scanned, the slides are heat-treated in a furnace at 375°C for one hour and rescanned at the same clay parameters stated above. This process aids in identifying the expandable, water-sensitive minerals.

When samples contain high levels of carbonates combined with low clay quantities, we may need to return to the sample and remove the carbonates to obtain a better clay scan for accurate identification and quantification.

Clay Mineral Identification and Quantification

Mixed-layer clays, particularly illite/smectite (I/S) are identified following the multiple peak method of Moore and Reynolds (1997). This entails measuring the 001/002 and 002/003 peaks of the illite/smectite. NEWMOD clay mineral generation program is used to create theoretical clay patterns, clay mixtures, and illite crystallinity. Identification of the amount of smectite (percent expandability) is also verified using the heat treated diffractogram overlain on the glycolated diffractogram in MDI Jade.

Kaolinite and chlorite are identified by the relative proportions of the peaks at 3.59 Å (kaolinite 002) and 3.54 Å (chlorite 004).

Clay mineral quantification includes: (1) the actual amount of discrete clay mineral species in the sample, and (2) the “expandability” or amount of smectite in mixed-layer clays, if present. Illite/Smectite (I/S) is the most common mixed-layer clay, but there are also chlorite/smectite (corrensite) and kaolinite/smectite. There are several tables in Moore and Reynolds (1997) that list 2θ positions and their correlative percent smectite in I/S (Table 8.3, p.273) or C/S (Table 8.4, p.281).

The Mineral Intensity Factor (MIF) method of Moore and Reynolds (1997) is applied to quantify the clay species. Weatherford has calculated MIFs for most clay minerals

encountered. The area of the specific mineral peak being used is divided by the MIF in the quantification process. The clay species is normalized to the total clay value derived from the bulk analysis.

References

- Bish D.L. and Reynolds R.C. Jr. (1989) Sample preparation for X-ray diffraction. Pp. 73-99 in: Modern Powder Diffraction (D.L. Bish and J.E. Post, editors) Reviews in Mineralogy, Volume 20, Mineralogical Society of America, USA.
- Drever, James I. (1973) The Preparation of Oriented of Clay Mineral Specimens for X-ray Diffraction Analysis by a Filter-Membrane Peel Technique.
- Hillier S. (2002b) Spray drying for X-ray powder diffraction specimen preparation. IUCR Commission on Powder Diffraction Newsletter No. 27. June 2002.
- Moore, D.M. and Reynolds, R.C. (1997) X-ray Diffraction and the Identification and Analysis of Clay Minerals, 2nd edition. Oxford University Press, Oxford, 332 pp.

References

- Ball, M.M. 1995. Permian Basin Province. *U.S. Geological Survey* 044. 1-21.
- Bureau of Economic Geology-The University of Texas at Austin. 2008. Project STARR Database. http://www.beg.utexas.edu/starr/ur_wolfberry.php. Web
- Blauer, R. E., I.N. Onat, and M.J. Lemieux. 1992. Production Data Indicate Reservoir and Fracture Performance in the Spraberry. *SPE* 23995: 503-512.
- Chukwuma, F. 2015. Nanopetrophysics of the Utica Shale, Appalachian Basin, Ohio, USA. M.S. Thesis, Department of Science, University of Texas at Arlington, USA.
- Clarkson, C.R., J.M. Wood, S.D. Aquino, M. Freeman, and V. Birss. 2012. Nanopore structure analysis and permeability predictions for a tight gas / shale reservoir using low-pressure adsorption and mercury intrusion techniques. *Spe* 155537: 1–18.
- DrillingInfo, 2016. www.drillinginfo.com
- Dutton, S. P., E.M. Kim, R.F. Broadhead, W.D. Raatz, C.L. Breton, S.C. Ruppel, and C. Kerans. 2005. Play analysis and leading-edge oil-reservoir development methods in the Permian Basin: Increased recovery-through advanced technologies. *AAPG Bulletin* 89.5 553–576.
- Gao, Z., Hu, Q., Peng, S., Ewing, R. 2012. Pore structure inhibits gas diffusion in the Barnett Shale. *AAPG Search and Discovery Article #50609*.

- Guevara, E.H. 2006 Mature petroleum reservoirs, significant remaining resources. Permian Basin Geophysical Society Presentation. Web.
- Hager, J. 1998. Steam drying of porous media. Ph.D. Thesis, Department of Chemical Engineering, Lund University, Sweden.
- Henry, J.. 2012. Wolfberry — Wolfcamp / Spraberry : How It Started. AAPG Conference and Exhibition presentation 110164.
- Hickman, R. G., R.J. Varga, and R.M. Altany. 2009. Structural style of the Marathon Thrust Belt, West Texas. *Journal of Structural Geology* 31. 900–909.
- Hills, J. 1972. Late Paleozoic sedimentation in West Texas Permian Basin. *AAPG Bulletin*. 2303–2322.
- Hu, Q., and R. Ewing. 2014. Integrated experimental and modeling approaches to studying the fracture-matrix interaction in gas recovery from Barnett Shale. Final Report, Research Partnership to Secure Energy for America (RPSEA), National Energy Technology Laboratory, Department of Energy, 91p.
- Hu, Q., R. Ewing, and H. Rowe. 2015a. Low nanopore connectivity limits gas production in the Barnett Formation. *Journal of Geophysical Research: Solid Earth*. Doi: 10.1002/2015JB012103.
- Hu, Q., W. Hu, Z. Gao, S. Liu, X. Liu, and W. Zhou. 2015b. Pore structure and tracer migration behavior of typical American and Chinese shales. *Petroleum Science*, 12(4): 651-663.

12(4): 651-663.

- Jarvie, D.M., 2012. Shale Resource Systems for Oil and Gas: Part 2 – Shale-oil Resource Systems. American Association of Petroleum Geologist Memoir 97, 89–119.
- Jarvie, D.M., R.J. Hill, T.E. Ruble, and R.M. Pollastro. 2007. Unconventional shale-gas systems: The Mississippian Barnett Shale of north-central Texas as one model for thermogenic shale-gas assessment. American Association of Petroleum Geologist Bulletin 91, 475–499.
- Katz, A., and A. Thompson. 1986. A quantitative prediction of permeability in porous rock. Physical Review B, 34: 8179–8181.
- Katz, A., and A. Thompson. 1987. Prediction of rock electrical conductivity from mercury injection measurements. Journal of Geophysical Research: Solid Earth, 92(B1): 599-607.
- Kaufmann, J. 2010. Pore space analysis of cement-based materials by combined nitrogen sorption - Wood's metal impregnation and multi-cycle mercury intrusion. Cement Concrete Comp. 32(7): 514-522.
- Kelly, L, J. Bachmann, D. Amoss, B. Angelico, B. Corales, B. Fernandez, P. Kissel, R. Roberts, and H. Stewart. 2012. Permian Basin: Easy to oversimplify, hard to overlook. Howard Weil Incorporated. Web.
- King, H.E., A.P.R. Eberle, C.C. Walters, C.E. Kliewer, D. Ertas, and C. Huynh. 2015. Pore architecture and connectivity in gas shale. *Energy and Fuels* 29.3: 1375–1390.

- Kuila, U., M. Prasad, A. Derkowski, and D.K. McCarty. 2012. Compositional controls on mudrock pore-size distribution: An example from Niobrara Formation. *SPE Annual Technical Conference and Exhibition 160141*: 16.
- Lohr, S., E. Baruch, P. Hall, and M. Kennedy. 2015. Is organic pore development in gas shales influenced by the primary porosity and structure of thermally immature organic matter? *Organic Chemistry*, 87: 119-132.
- Mayer, R. P., and R. A. Stowe. 1965. Mercury porosimetry-breakthrough pressure for penetration between packed spheres. *Journal of Colloid Science*. 20 Vol. Academic Press, Web. 28 Nov. 2016.
- Micrometrics. 2011. Autopore IV 9500 Operators Manual.
- Mohan, K., and P. Leonard. 2013. Evaluating EOR Techniques in the Spraberry. *SPE 168750/URTeC 1579528* 12–14.
- Montgomery, S. L., D. S. Schechter, and J. Lorenz. 2000. Advanced reservoir characterization to evaluate carbon dioxide flooding, Spraberry Trend, Midland Basin, Texas. *AAPG Bulletin* 84: 1247–1273.
- Murchison Oil & Gas, Inc. 2010. Geographic Footprint. Released on January 1, 2010. Available at <http://www.murchisonoil.com/about/permian-basin.html>. Accessed 25 June 2016
- Putra, E., and D. Schechter. 1999. Reservoir simulation of a waterflood pilot in the naturally fractured Spraberry Trend. *SPE 54336*: 1-15.

- Raji, M., D. R. Grocke, C. Greenwell, and C. Cornford. 2015. Pyrolysis, porosity, and productivity in unconventional mudstone reservoirs: free and adsorbed oil. *SPE-178685-MS/URTeC:2172996*: 1-11.
- Schechter, D., and T. Yocham. Overview of the CO₂ Pilot in the Spraberry Trend Area. New Mexico Institute of Mining and Technology.
- Schlumberger. 2014. sCore Lithofacies Classification Reveals Barnett Reservoir Quality. Case Study. www.slb.com/ls
- Swanson, B. 1981. A simple correlation between permeabilities and mercury capillary pressures. *Society of Petroleum Engineers*, 33(12) 2498-2504.
- Wang, S., F. Javadpour, and Q.H. Feng. 2016. Confinement correction to mercury intrusion capillary pressure of shale nanopores. *Scientific Reports*, 6: 20160, doi: 10.1038/srep20160.
- Webb, P.A. An introduction to the physical characterization of materials by mercury intrusion porosimetry with emphasis on reduction and presentation of experimental data. Micromeritics Instrument Corporation. 2001.
- Zhou, J., G. Ye, and K. Breugel. 2010. Characterization of pore structure in cement-based materials using pressurization-depressurization cycling mercury intrusion porosimetry (PDC-MIP). *Cement and Concrete Research*, 40 (7): 1120-1128.

Biographical Information

Ryan Quintero is from Richmond, Texas and attended high school in Sugarland, Texas. He graduated with a Bachelors of Science degree in Geology from the University of Texas at San Antonio in 2012. After working in the petroleum industry for three years he began pursuing a Masters of Science degree in Petroleum Geology at the University of Texas at Arlington and graduated in December of 2016. He is a first generation college graduate of both a BS and MS degree.